POSITION RESOLUTION IN CRYSTAL CALORIMETER

Mudathir FAKHRELDIN OSMAN YAHYA

T.C.
BURSA ULUDAĞ UNIVERSITY
GRADUATE SCHOOL OF NATURAL AND APPLIED SCIENCES

POSITION RESOLUTION IN CRYSTAL CALORIMETER

Mudathir FAKHRELDIN OSMAN YAHYA
0000-0001-5214-328X

Asst. Prof. Dr. Fatma KOÇAK
(Supervisor)

MSc THESIS
DEPARTMENT OF PHYSICS

BURSA – 2021
All Rights Reserved

ÖZET

Yüksek Lisans Tezi

KRİSTAL KALORİMETREDE KONUM ÇÖZÜNÜRLÜĞÜ

Mudathir FAKHRELDIN OSMAN YAHYA

Bursa Uludağ Üniversitesi
Fen Bilimleri Enstitüsü
Fizik Anabilim Dalı

Danışman: Dr. Öğr. Üyesi Fatma KOÇAK

LYSO kristalinin, hızlı bozunma süresine, yüksek ışık verimine, küçük Molière yarıçapına sahip olması ve radyasyona dayanıklılığı gibi temel özelliklerinden dolayı Türk Hızlandırıcı Merkezi Parçacık Fabrikası dedektörünün elektromanyetik kalorimetre (THM-PF EKAL) ünitesinde kullanılması önerilmektedir. Bu çalışmada, 3×3 LYSO matrisinden oluşan bir kalorimetreye gönderilen bir elektron tarafından başlatılan elektromanyetik sağanağın ağırlık merkezinin konumunu belirlemek için ağırlık merkezi yöntemi kullanıldı. Kalorimetre, her birinin ön ve arka yüzü 25 mm × 25 mm olan, 200 mm uzunluğunda dokuz kristalden oluşmaktadır. 0,1 GeV ile 2 GeV aralığında enerjilere sahip elektronlar için, kalorimetre prototipinin performansı incelenmiştir. GEANT4 Monte Carlo simülasyonu kullanılarak, kristal matrisinin merkezindeki kristale dik olarak gönderilen bir elektron için elektromanyetik kalorimetrenin konum çözünürlüğü, x-ekseni doğrultusunda $\sigma_x = ((2{,}77 \pm 0{,}07)/\sqrt{E}) \oplus (1{,}46 \pm 0{,}10)$ mm ve y-ekseni doğrultusunda $\sigma_y = ((2{,}77 \pm 0{,}05)/\sqrt{E}) \oplus (1{,}31 \pm 0{,}07)$ mm olarak elde edilmiştir. Ayrıca, EKAL modülünün iki boyutlu konum çözünürlüğü, kristalin merkezinde $\sigma_R = ((3{,}95 \pm 0{,}08)/\sqrt{E}) \oplus (1{,}91 \pm 0{,}11)$ mm olarak hesaplanmıştır.

Son olarak, kristal matrisinin yüzeyine çeşitli açılarda elektronlar gönderilerek konum çözünürlüğünün elektronun geliş açısına bağlı değişimi incelenmiştir. LYSO matrisine gönderilen elektronun geliş açısı arttıkça konum çözünürlüğünün bozulduğu ve en iyi konum çözünürlüğünün elektron matris yüzeyine dik olarak gönderildiğinde elde edildiği gözlemlenmiştir.

Anahtar kelimeler: GEANT4 simülasyonu, kalorimetre, konum çözünürlüğü, kristal.

2021, x + 68 sayfa.

ABSTRACT

MSc Thesis

POSITION RESOLUTION IN CRYSTAL CALORIMETER

Mudathir FAKHRELDIN OSMAN YAHYA

Bursa Uludağ University
Graduate School of Natural and Applied Sciences
Department of Physics

Supervisor: Asst. Prof. Dr. Fatma KOÇAK

LYSO crystal, because of its major properties for instance, fast decay time, high light yield, small Molière radius and good radiation hardness, is proposed to be used for the electromagnetic calorimeter unit of Turkish Accelerator Center Particle Factory detector (TAC- PF ECAL). In this study, the center of gravity method was used to determine the position of the center of gravity of the electromagnetic shower initiated by an electron sent to a calorimeter consisting of a 3×3 LYSO matrix. The calorimeter consists of nine 200 mm long crystals, each with 25 mm × 25 mm front and backside faces. The performance of a calorimeter prototype consists of LYSO crystal scintillators has been measured at normal incidence by electron having energies between 0.1 GeV and 2 GeV. The position resolution of the TAC-PF electromagnetic calorimeter for an electron injected perpendicular to the central crystal is parameterized by means of GEANT4 Monte Carlo simulation as $\sigma_x = ((2.77 \pm 0.07)/\sqrt{E}) \oplus (1.46 \pm 0.10)$ mm in the x-axis direction, and $\sigma_y = ((2.77 \pm 0.05)/\sqrt{E}) \oplus (1.31 \pm 0.07)$ mm in the y-axis direction. Also, simulated position resolution in the two-dimensional prototype of ECAL is found to be $\sigma_R = ((3.95 \pm 0.08)/\sqrt{E}) \oplus (1.91 \pm 0.11)$ mm at the center of the central crystal.

Finally, electrons are sent at various angles to the surface of the crystal matrix and the variation of position resolution depending on the electron incidence angle is investigated. It has been observed that the position resolution deteriorates as the incidence angle of the electron sent to the LYSO matrix increases and the best position resolution is obtained when the electron is sent perpendicular to the matrix surface.

Key words: Calorimeter, crystal, GEANT4 simulation, position resolution**.**

2021, x + 68 pages.

ACKNOWLEDGEMENT

I would like first to acknowledge the amazing support, monitors, and guidance from my supervisor Asst. Prof. Dr. Fatma KOÇAK. She always gives me constructive comments and warm encouragement. Her guidance helped me at all the time of research and writing of this thesis. Also, I have greatly benefited from Ahmed SAAD. Without their guidance and persistent help, this thesis would not have been possible.

Besides my supervisor, I would like to show my gratitude to Assoc. Prof. Dr. Cem Salih ÜN and Asst. Prof. Dr. Zerrin KIRCA for their valuable classes.

I want to offer special thanks to Tasneem SALAH for her constant encouragement throughout my research period. Last but not the least, I would like to thank my parents for supporting me spiritually throughout my life.

The numerical calculations reported in this thesis was performed at TUBITAK ULAKBIM, High Performance and Grid Computing Center (TRUBA Resources).

Mudathir FAKHRELDIN OSMAN YAHYA
…/09/2021

CONTENTS

Pages

ÖZET i
ABSTRACT ii
ACKNOWLEDGEMENT iii
SYMBOLS and ABBREVIATIONS v
FIGURES viii
TABLES x
1. INTRODUCTION 1
2. THEORETICAL BASICS and LITERATURE REVIEW 4
2.1. High Energy Physics Detectors 4
2.1.1. Element of high energy physics detector 4
2.2. Calorimetry 5
2.2.1. Electromagnetic calorimeters 6
2.2.2. Hadronic calorimeter 13
2.3. Interactions of Charged Particles with Matter 15
2.3.1. Bremsstrahlung 15
2.3.2. Ionization and excitation 17
2.4. Interactions of Photons 19
2.4.1. Photoelectric effect 20
2.4.2. Compton effect 21
2.4.3. Pair production 22
2.5. Crystals in High Energy Physics Detectors 24
2.5.1. Crystal's detection mechanisms 27
2.5.2. Inorganic crystal scintilators 28
2.6. Position Resolution 31
3. MATERIALS and METHOD 33
3.1. Turkish Accelerator Center (TAC) 33
3.2. GEANT4 Simulation Program 35
3.2.1. Overview of GEANT4 35
3.2.2. General structure of GEANT4 36
3.2.3. GEANT4 simulation units 38
3.3. TR- Grid (TRUBA) System 39
4. RESULTS and DISCUSSION 42
5. CONCLUSION 61
REFERENCES 63
RESUME 67

SYMBOLS and ABBREVIATIONS

Symbols	Definition
σ_i	Atomic Cross-Section
A	Atomic Number
Z	Avogadro Number
$X_{gravity}$	Center of Gravity in x Coordinate
$Y_{gravity}$	Center of Gravity in y Coordinate
z	Charge Number of the Incident Particle
r_e	Classical Electron Radius
$\sigma_{Compton}$	Compton Scattering
b	Constant Term
E_c	Critical Energy
δ	Density Effect
f_{em}	Electromagnetic Component
e^-	Electrons
m_e	Electron Mass
E_i	Energy Deposited in the ith Crystal
E	Energy of the Incident Particle
E_0	Initial Energy
I_0	Initial Intensity
γ	Lorentz Factor
μ	Mass Attenuation Coefficient
M	Mass of the Incident Particle
I	Mean Distance
λ_{int}	Mean Excitation Energy
K_{NUC}	Nuclear Interaction Length
κ_e	Pair Production (Electron Field)
σ_{Pair}	Pair Production (Nuclear Field)
$\sigma_{P.e}$	Pair Production Cross-Section
$\sigma_{g.d.r}$	Photoelectric Effect
σ_x	Photonuclear Interactions
σ_y	Position Resolution in x Coordinate
e^+	Position Resolution in y Coordinate
e^-	Positron
X_0	Radiation Length
X_j	Radiation Length for the jth Element
$\sigma_{Rayleigh}$	Rayleigh Scattering
β	Relativistic Velocity of the Particle
θ_γ	Scattering Angle of the Incident Photon
a	Stochastic Term
σ_R	Two-Dimensional Position Resolution
W_j	Weight for the jth Element
A	Weight of the Material
x_i	x Coordinate of the Center of the ith Crystal
y_i	y Coordinate of the Center of the ith Crystal

Abbreviations	Definition
Ar	Argon
BaF_2	Barium Fluoride
BGO	Bismuth Germanite
$Bi_4Ge_3O_{12}$	Bismuth Germanium Oxide
CeF_3	Cerium Fluoride Crystal
CsI	Cesium Iodide
CP	Charge Conjugation (C) and Parity (P)
COMET	COherent Muon to Electron Transition
CDF	Collider Detector at Fermilab
CMS	Compact Muon Solenoid
DRDC	Detector Research and Development Committee
DTL	Drift Tube LINAC
EM	Electromagnetic
ECAL	Electromagnetic Calorimeter
CERN	European Organization for Nuclear Research
FEL	Free-Electron Laser (FEL) Facility
GEANT4	GEometry ANd Tracking
HEP	High Energy Physics
IR FEL	Infrared Free Electron Laser
IP	Interaction Point
J-PARC	Japan Proton Accelerator Research Complex
Kr	Krypton
LEP	Large Electron–Positron Collider
LHC	Large Hadron Collider
PbO	Lead Glass
PWO ($PbWO_4$)	Lead Tungstate
LINAC	Linear Particle Accelerator
LSO	Lutetium Oxyorthosciilicate
LYSO	Lutetium-Yttrium Oxyorthosilicate
MW	Megawatt
NOMAD	Neutrino Oscillation Magnetic Detector
OPAL	Omni-Purpose Apparatus at LEP
PS	Polystyrene
PVT	Polyvinyl Toluene
PAF	Proton Accelerator Facility
PAF-HE	Proton Accelerator Facility- High Energy
PAF-LE	Proton Accelerator Facility- Low Energy
QCD	Quantum Chromodynamics
RFQ	Request for Quotation
RMS	Root Mean Square
SASE	Self-Amplified Spontaneous Emission (SASE)
SM	Standard Mode
SLAC	Stanford Linear Accelerator Center
SPS	Super Proton Synchrotron
SSM	Superconducting Solenoid Magnet
TMP	Tetramethyl Pentane

CsI(Tl)	Thallium Activated Cesium Iodide
NaI(Tl)	Thallium Activated Sodium iodide
TARLA	Turkish Accelerator and Radiation Laboratory
TAC	Turkish Accelerator Center
TAC-PF	Turkish Accelerator Center-Particle Factory
TRUBA	Turkish National Science e-Infrastructure
UV	Ultraviolet
Xe	Xenon

FIGURES

Page

Figure 2.1. Characteristic design of a high energy physics detector at a colliding beam experiment 5
Figure 2.2. Sketch of a simple model for shower parametrization 7
Figure 2.3. Critical energy for the electron in chemical elements. The solid line displays the fits for liquids and solids materials while dashed line displays the fit for gases 9
Figure 2.4. Dual descriptions of the critical energy E_c 9
Figure 2.5. Difference between the experimental results on the electromagnetic calorimeter part of pion cascades in lead and copper calorimeters. 14
Figure 2.6. Longitudinal shower profiles for four different cascades initiated by 270 GeV pions 15
Figure 2.7. Bremsstrahlung cross - section $k\,d\sigma_{LPM}/dk$ in the lead as a function of the fraction of momentum taken by the radiated photon 16
Figure 2.8. Energy loss per radiation length in the lead as a function of positron or electron energy 18
Figure 2.9. Intervals in which interactions dominate as a function of the photon energy and the Z of absorber material. 20
Figure 2.10. Kinematic variables in Compton scattering 21
Figure 2.11. Cumulative cross-sections for photon energy in lead and carbon. 24
Figure 2.12. A comprehensive photon range calculated at the ψ by the sodium iodide doped with thallium scintillators at SLAC experiments 25
Figure 2.13. The estimated Higgs mass peak reformed from its 2 photon decays measured by the Compact Muon Solenoid lead tungstate calorimeter 26
Figure 2.14. The obtained energy resolution for the incident electron for L3 BGO calorimeter measured at CERN (Left). The obtained energy resolution of Bhabha electrons identified by the L3 BGO calorimeter at LEP (Right) 26
Figure 2.15. Demonstrates the variance in polarization for $v < c/n$ and $v > c/n$, and geometric angle of the Cherenkov radiation 27
Figure 2.16. Light yield as a function of integration time for 5 quick (Left) and 5 slow (Right) crystal scintillators calculated by XP2254b PMT 30
Figure 2.17. Left: the excitation and emission ranges (dashed and thick solid line), right: the transmittance ranges for wavelength spectrum for 8 different crystal scintillators 31
Figure 3.1. Diagram vision of TAC ERL-Ring Super Charm Factory 34
Figure 3.2. Class category diagram of GEANT4 37
Figure 3.3. Step definition 39
Figure 4.1. 3×3 LYSO crystal matrix 42
Figure 4.2. Relation between $x_{gravity}$ and $y_{gravity}$ in the center of LYSO matrix for 0.5, 1, 1.5, and 2 GeV electrons 43
Figure 4.3. Position obtained by $x_{gravity}$ vs. x_{true} for 0.5, 1, 1.5, and 2 GeV electrons. the S-curve represented with solid blue line 44

Figure 4.4. Position obtained by $y_{gravity}$ vs. y_{true} position for 0.5, 1, 1.5, and 2 GeV electrons. the S-curve represented with solid blue line 45
Figure 4.5. S-shape correction $x_{corrected}$, for electron having energy of 500 MeV, 1 GeV, 1.5 GeV, and 2 GeV 48
Figure 4.6. S-shape correction $y_{corrected}$, for electron having energy of 500 MeV, 1 GeV, 1.5 GeV, and 2 GeV 49
Figure 4.7. Dependency of the corrected position ($x_{corrected}$) in LYSO scintillators on the impact position (x_{true}) 50
Figure 4.8. Dependency of the corrected position ($y_{corrected}$) in LYSO scintillators on the impact position (y_{true}) 51
Figure 4.9. Obtained position resolutions in x coordinates at the central crystal of the 3×3 LYSO matrix as a function of electron energies. The lines are the fits of the data. The error bars are smaller than the symbols presented 52
Figure 4.10. Obtained position resolutions in y coordinates at central 3×3 matrix LYSO as a function of electron energy. The solid lines represent the fits of the data. The error bars are smaller than the symbols presented 53
Figure 4.11. Obtained position resolution in two-dimensional as a function of electron energy 55
Figure 4.12. Calculated position resolutions as a function of electron impact position in the x and y coordinates. 56
Figure 4.13. S-like curves for 5 degrees incident angle at 0.5 GeV 56
Figure 4.14. Variation of position resolution normalized to position resolution at zero degrees as a function of the electron incidence angle. The solid lines represent the fit results 57
Figure 4.15. Calculated position resolutions as a function of inverse square root of electron's energy at the central LYSO crystal 58
Figure 4.16. Position resolution versus the true position, for electron energies of 1 and 2 GeV at normal and 15 degrees incidence. 59
Figure 4.17. Position resolutions obtained from the GEANT4 simulation and the COMET ECAL prototype in Ref (Oishi, 2014) 60

TABLES

Page

Table 2.1. Main properties of heavy crystal scintillators 30
Table 3.1. Primary Factors of TAC PF Facility……...……..35
Table 4.1. Calculation results of the c, d and e parameters of the position resolution for 3×3 LYSO matrix for different energies in x coordinates……...46
Table 4.2. Calculation results of the c, d and e parameters of the position resolution for 3×3 LYSO matrix for different energies in y coordinates 47
Table 4.3. The fit parameters of position resolution for different incidence positions of electrons in x coordinates. 53
Table 4.4. The fit parameters of position resolution for different incidence positions of electrons in y coordinates. 54
Table 4.5. The fit parameters of position resolution for different incidence positions of electrons in two dimensions 55
Table 4.6. Position resolution obtained for various incidence angles at the center of the central crystal. A sample of 10000 events was used for each energy 57

1. INTRODUCTION

Elementary particle physics can be defined as the study and search of matter's fundamental constituents. At present, the noblest theory for recognizing matter and three out of the basic four forces, specifically, the electromagnetic interactions, strong and weak interactions, is the Standard Model of Particle Physics. That means the Standard Model (SM) of elementary particle physics explains the fundamental interactions of subatomic particles. The electroweak theory described the electromagnetic and weak interactions (Salam, 1979; Weinberg, 1980), while Quantum Chromodynamics (QCD) depicted the strong interaction (Gell-Mann, 1962).

In addition to experimentations with cosmic rays, smashing particles in particle accelerators have appeared to be a significant tool for physicists to study and confirm the Standard Model's predictions over years. These experiments are carried out with well-built accelerators and contemporary particle detection techniques. The search of the matter's fundamental constituents demands large particle colliders such as the Large Hadron Collider (LHC), which accelerate a variety of particles including electron, positron, or proton beam to very high energies. The collision can arise among two accelerated particle beams or amid the colliding beam and a fixed target. After the collision, new-generated particles and their interactions are explored in the detectors constructed around the interaction point (IP) (Grupen & Schwartz, 2008). The detectors for the experiments at high-energy colliders are constructed to detect and measure the particles generated at collisions. Each collision makes an event at a definite IP. The classification of the particles formed in each event by evaluating their four-momenta is the subject of high energy physics studies. Large particle detectors are enfolding the majority of the 4π zone around the interaction point. These contemporary detectors entail several layers of sub-detectors, each planned to accomplish specific measurements (Frass & Wlaczak, 2009).

The electromagnetic calorimeters (ECAL) which are optimized to determine the energy of charged and neutral particles, are one of the most important parts of the High Energy Physics (HEP) detectors. To measure the position and energy of the electrons or photons, ECALs which are made of inorganic scintillators are commonly employed in

HEP experiments. The deposited energies in several crystals are used to determine the position of a particle, while the total deposited energy in the calorimeter is exploited to calculate the energy of the incident particle (Kocak, 2015).

Initially, silicate doped with cerium-based heavy scintillator crystals have been industrialized for medical applications. The scintillation characteristics of lutetium oxyorthosilicate (LSO) (Melcher & Schweitzer, 1992) and lutetium yttrium oxyorthosilicate (LYSO) (Cooke et al., 2000; Kimble, Chou & Chai, 2002) are discovered later. LYSO scintillation crystals have high stopping power (> 7 g/cm^3), high light yield (200 times of PWO) and fast decay time (40 ns), and excellent radiation hardness against gamma rays, neutrons, and protons (Mao, Zhang & Zhu, 2009). Moreover, LYSO scintillators produce light in the wavelength ranging between 360 to 600 nm and peaking at 402 nm. Because of all the aforementioned advantages, this material has also drawn broad interest in experimental HEP research groups in advancing the electromagnetic calorimeters performance such as the proposed SuperB forward endcap calorimeter (Eigen et al., 2013), the KLOE experiment (Cordelli et al., 2011), and the Muon-to-Electron (Mu2e) experiment (Oishi, 2014). LYSO crystal scintillators have been also studied for the ECAL unit of the Turkish Accelerator Center-Particle Factory (TAC-PF) detector, along with CsI(Tl) and PWO scintillators (Kocak & Tapan, 2017).

To obtain high energy and best position resolutions in electromagnetic calorimeter units of HEP detectors, crystal scintillators are generally preferred. These crystals are inorganic scintillators such as PWO, CsI, CsI(Tl), and LYSO. When electrons or photons with very high energy enter the crystal, they lose their energy by creating an electromagnetic shower inside the crystal. One of the most used methods to determine the coordinates of the particle hitting the crystal surface is the center of gravity method. Using this method, the position resolution of the incident particle can be calculated with the following equations:

$$X_{gravity} = \frac{\sum_i x_i E_i}{\sum_i E_i}$$

for the x-axis, and

$$Y_{gravity} = \frac{\sum_i y_i E_i}{\sum_i E_i}$$

for the y-axis.

Where E_i stands for the energy deposited in the ith LYSO crystal and (x_i y_i) stand for x and y position of the center of the ith LYSO block at the reference plane (Wigmans, 2000).

In this study, using the GEANT4 package, a calorimeter geometry in matrix form is created and the energies deposited in the crystals are obtained. Turkish National Science e-Infrastructure (TRUBA) is used for calculations that have been made with the GEANT4 simulation. The ROOT analysis package is used for the analysis of the data obtained from the simulation and the fits. Position resolution was determined for incident electrons that have energy varying from 100 MeV to 2 GeV, calculations are made for the LYSO crystal, which has been recently proposed to be used in many HEP experiments due to its radiation hardness and many other properties. Depending upon the energy and impact position angle of the electron coming to the crystal surface, the changes in the position resolution are studied.

2. THEORETICAL BASICS and LITERATURE REVIEW

2.1. High Energy Physics Detectors

2.1.1. Element of high energy physics detectors

The search of the matter's fundamental constituents demands large particle colliders like LHC to accelerate particles like electron, positron, or proton beams and bring them into collision at the possible highest energy. The collision can arise among two accelerated particle beams (head-on collision) or amid the colliding beam and a fixed target. After the collision, new-generated particles and their interactions are analyzed in the detectors constructed around the interaction point (IP). Many detection principles are being applied in HEP. Gaseous detectors, solid-state detectors, and scintillator detectors are the most common techniques. The gaseous detectors are based on the electron-ion pairs (ionization) produced by a charged particle as it transforms across the material. Solid-state detectors employ semiconductor materials, for example, silicon or germanium. In contrast to the gaseous detectors, charged particles produce electron-hole pairs in the solid-state detectors. In scintillators, photons are converted when an electron returns to its ground state (excitation mechanism). Scintillations are then detected by photomultiplier tubes or photodiodes, which transfer them to electrical signals. Depending on the physics objectives of the experiment, a detector in particle colliders could implement the various technologies mentioned above (Grupen & Schwartz, 2008). A typical colliding beam detector used on a collider contains a vertex detector, tracker, calorimeter, and muon detector. A schematic view of a characteristic HEP detector structure is demonstrated in Figure 2.1, presenting all sub-detectors (Moser, 2009).

The HEP detectors each have a detection system built for a specific purpose of the experiment. Generally, a HEP detector should have the following characteristics:

- Measuring the charges, scattering directions, and momentum of the particle created after the collision.
- Measuring the energy carried by electrons, photons, and hadrons (protons, pions, neutrons, etc.) scattered in all directions in the collision.

- Detecting muons that occur in the collision.
- Detecting the presence of particles such as neutrinos that cannot be detected by using momentum conservation.
- Must have the ability to provide the above-mentioned information quickly enough and be able to record the measurements.
- It should be resistant to radiation damage (Koçak, 2010).

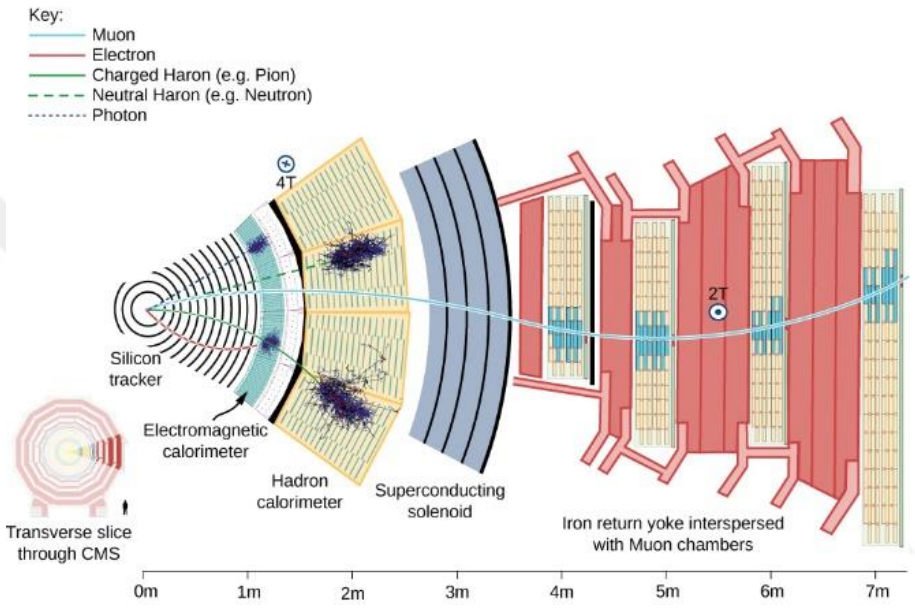

Figure 2.1. Characteristic design of a high energy physics detector at a colliding beam experiment (Sirunyan et al., 2017).

2.2. Calorimetry

Calorimetry is a widespread detection concept in HEP. Initially designed to ponder cosmic-ray phenomena, this strategy is used in accelerator-based HEP experiments for the determinations of photons, electrons, and hadrons energy. Calorimeters are pieces of instruments item in which absorbs the electrons and photons to convert their energy to a detectable signal. The interaction of the incident particle with the materials of the detector creates a secondary particle while the energy of incident particles decreases gradually. The deposited energy by charged particles showered in the calorimeter's active layer, which can be spotted in the kind of light or charge, acts as energy measures of the injected particles. Generally, electromagnetic calorimeters, detect charged

particles within their electromagnetic interactions, and hadronic calorimeters spot hadrons by means of their electromagnetic and strong interactions. Additionally, calorimetry can be divided according to their structure method to homogeneous and sampling calorimeters. Sampling calorimeters are made of an absorber to absorb the energy of incident particles, and an active part to present the measurable signal. On the other hand, homogeneous calorimeters are made from a single material to act as an absorber and active layer (Fabjan & Gianotti, 2003).

2.2.1. Electromagnetic calorimeters

Photons and electrons interact with material through QED interactions, despite the complicated phenomenology of cascade growth in a matter, the main characteristics of the shower can be calculated with simple, practical equations. Two notable procedures can be recognized. For energies greater than 10 MeV, Bremsstrahlung is the leading cause of energy loss of the electron. While at the same energy range, the photon yields electron-positron pair production primarily. For energies exceeding 1 GeV, these processes release the same amount of energy approximately. At low energies, electrons lose energy mostly throughout collisions with molecules and the atoms of the matter, which results in excitation and ionization. Photons lose energy via photoelectric and Compton effect. As a result, electrons and photons of adequately more than 1 GeV energy deposited on a material generate secondary electrons and positrons by pair productions or secondary photons by Bremsstrahlung. In turn, these secondary particles create further particles by the same processes, therefore providing growth to a cascade of particles of gradually decreasing energies (see Figure 2.2). The number of particles in the cascade rises up till the electron component's energy drops under a critical energy, where energy is mostly degenerate by excitation and ionization instead of producing extra particles.

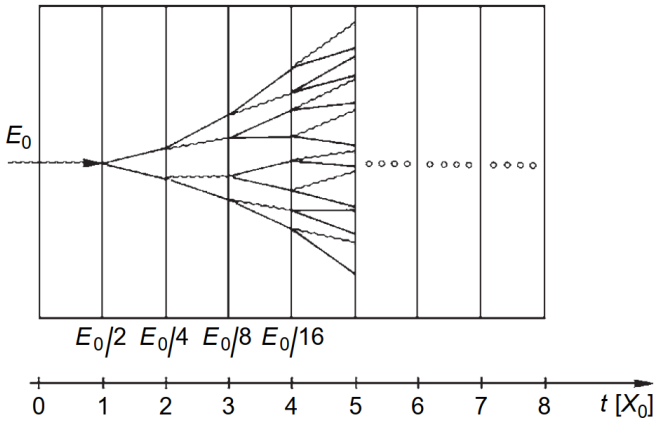

Figure 2.2. Sketch of a simple model for shower parametrization (Grupen & Schwartz 2008).

Radiation length: The main longitudinal and lateral sizes of electromagnetic cascades can be expressed by one parameter, the radiation length X_0, which changes according to the properties of the substance (Hagiwara et al., 2002).

$$X_0 = \frac{716\ g\ cm^{-2} A}{Z(Z+1)\ln(287/\sqrt{Z})} \tag{2.1}$$

Here A and Z stand for the weight of the material and atomic number, respectively. Radiation length dominates the proportion at which electrons lose energy by the Bremsstrahlung process as it characterizes the mean distance x that an electron has to move in a matter to decrease original energy E_0 by 1/e.

$$\langle E(x) \rangle = E_0 e^{-x/X_0} \tag{2.2}$$

Likewise, the initial intensity I_0 of a photon beam crossing a matter is generally absorbed within pair-production process. Once covering a distance $x = (7/9)X_0$, its intensity is decreased by 1/e from initial intensity,

$$\langle I(x) \rangle = I_0 e^{(x/X_0)(7/9)} \tag{2.3}$$

Radiation length in a combination of material or compound can be approached as.

$$1/X_0 = \sum w_j/X_j \tag{2.4}$$

Where w_j and X_j are the fraction by weight and the radiation length for the jth component (Desler & Edwards, 2005).

Critical energy: to describe critical energy ϵ, two different characterizations can be used. First, it is defined as the energy at which energy losses by ionization and bremsstrahlung become equivalent. This energy differs according to the structures of the substance and is given by

$$\mathrm{E}_c = \frac{710(610)\mathrm{MeV}}{\mathrm{Z} + 0.92(1.24)} \tag{2.5}$$

for (solids) gases, as shown in Figure 2.3.

In the second explanation, critical energy E_c is energy at which the electron energy E equivalents to ionization loss per X_0:

$$\frac{dE}{dx}(\text{ionization}) = \frac{E}{X_0} \tag{2.6}$$

The two definitions are equal in the approximation (Fabjan & Gianotti, 2003).

$$\frac{dE}{dx}(\text{bremsstrahlung}) \cong \frac{E}{X_0} \tag{2.7}$$

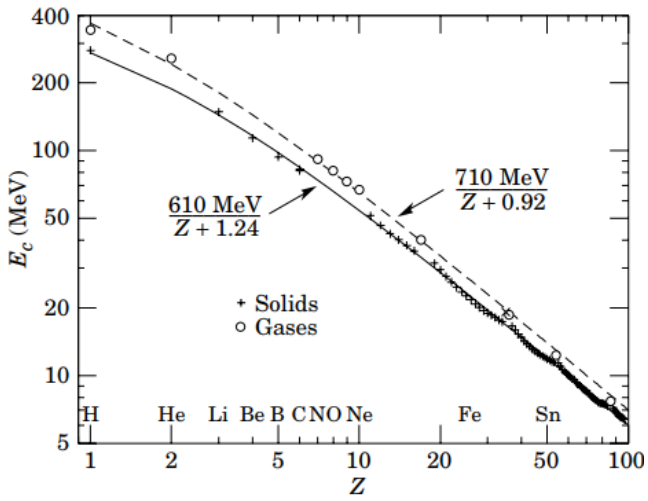

Figure 2.3. Critical energy for the electron in chemical elements. The solid line displays the fit for solids materials while dashed line displays the fit for gases (Desler & Edwards, 2005).

Figure 2.4 displays these definitions in the case of copper, the critical energy equals to 19.63 MeV in the copper.

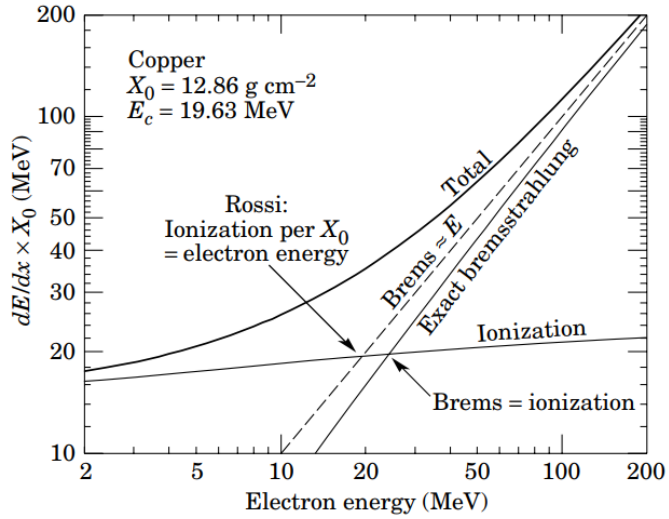

Figure 2.4. Dual descriptions of the critical energy E_c (Desler & Edwards, 2005).

- Main Techniques Examples and Facilities of EM Calorimeters

The main methods applied to construct sampling and homogeneous electromagnetic calorimeters will be discussed in this part. Information about the interactions of particles

with matter will be given and types of detectors in process or in formation will be mentioned.

- Homogeneous calorimeters

These detectors provide outstanding energy resolution, because the incident particles entire energy is dropped in active layers. However, the main disadvantage of this type of calorimeters is being less longitudinally and laterally subdivided, when position resolutions and classification of the particles are required. Moreover, because these machines are non-compensating, appropriate materials possess a long interaction length, therefore making the detector with a required width to hold hadron cascades is high-priced. In accelerator experiments, homogeneous calorimeters are rarely employed as hadronic calorimeters. Usually, they are used in astroparticle and neutrino physics researches in which considerable dimensions are desirable to discover infrequent incidents.

Homogeneous calorimeters generally can be separated into four groups:

Semiconductor calorimeters: Electron-hole pairs are produced in the semiconductor material. An electric field is applied to the semiconductor and the produced charge carriers are collected and converted to an electric signal. Exceptional energy resolution can be obtained by these kinds of detectors. The most common materials used in these detectors are germanium and silicon crystals which are employed in a lot of nuclear physics applications.

Cherenkov calorimeters: In this type of detectors relativistic electrons or photons moving in a medium of translucent material emit photons called Cherenkov photons. Therefore, the produced signals are accumulated as light. For instance, electromagnetic calorimeters made of Lead-glass (PbO) are vastly used in HEP experiments. Lead-glass calorimeters are inexpensive and easy to approach and consequently have been broadly employed in HEP purposes in the past, for instance, in the OPAL experiment at LEP (Akrawy et al., 1990) and in the NOMAD neutrino experimentation at the CERN SPS (Altegoer et al., 1998).

Scintillator calorimeters: In this calorimeter a fluorescence is produced by ionization tracks in the active medium of the detector. The most commonly used crystals for HEP purposes are: thallium-doped sodium-iodide scintillators (NaI(Tl)) which have been generally utilized for their significant light yield and soft cost. Nevertheless, it has a quite long radiation length and hygroscopic crystals, thus it is not appropriate for big experiments wherever more solid crystals are needed such as $PbWO_4$ and BGO, which tolerate very compact detectors are perfect. Cesium Iodide (CsI) crystals are being widely employed by the CLEO experiment (Bebek, 1988), BaBar experiment (Boutigny et al., 1995), KTeV (Alavi-Harati et al., 1999) experiment, and Belle experiment (Abashian et al., 2002). Lastly, lead tungstate ($PbWO_4$) crystals, which are very fast, strong radiation hardness, and dense, are well-matched to the LHC and has been implemented by the CMS experimentation (CMS Collaboration, 1997).

Noble liquid calorimeters: Noble gases such as Argon or Xenon act as active medium for the detectors. These gases are functioned at cryogenic temperature. Even though ionization and scintillation signals can be compiled in this case, major calorimeters for HEP experiments are constructed to measure the charge. For example, liquid krypton was used as the electromagnetic calorimeter in the NA48 experiment at CERN (Fanti et al., 1999). Obtained signals are gathered in the shape of Cherenkov or scintillation photons in this type of detectors. These photons can be transformed into photoelectrons by a photo sensitive system such as an avalanche photodiode or photomultiplier (Fabjan & Gianotti, 2003).

- Sampling calorimeters

According to nature of the detector's active layer, sampling calorimeters can be categorized into solid-state calorimeters, liquid calorimeters, and gas calorimeters, in which signals are collected as electric charges, which scintillation calorimeters, in this case, the signals are gathered in the shape of light.

Scintillation sampling calorimeters: This type of calorimeters employs organic scintillators organized in form of plates or fibers. These calorimeters are comparatively economical, can be constructed in a significant geometry, and effortlessly divided, has

an adequate light yield with quick response, and can be created by appropriately modifying the percentage of the scintillator and absorber volumes. This type of calorimeters is used in the CDF experiment (Balka et al., 1988; Bertolucci et al., 1988), ZEUS experiment (Group et al., 1990).

Gas sampling calorimeters: Primarily because of the low price and division flexibility of these type of calorimeters, they have been broadly used till very recent LEP experiments. Nevertheless, since they provide low energy resolution due to numerous factors such as path length dissimilarities and Landau fluctuations impact in the active medium, they are not considered for the present and future detectors. As an example, sampling gas ECAL was utilized in the ALEPH experiment at LEP. (Fabjan & Gianotti, 2003).

Solid-state sampling calorimeters: Silicon acts as an active layer in most sampling solid-state calorimeters. The major benefit of these detectors is that the active medium's density exceeds the sampling gas calorimeters by thousand times, which provides the creation of alternative compact machines in addition to a better ratio between signal and noise. This is because only 3.6 electron volt is required to yield an electron-hole pair in silicon, in contrast to 30 electron volts in gas. Consequently, solid-state detectors function with unity gain, which sidesteps the obstacle of charge reduplication. Tungsten as, a dense absorber, have been broadly used in in compact silicon calorimeters to monitors luminosity in LEP detectors.

Liquid sampling calorimeters: Warm-liquid as tetramethyl pentane (TMP) calorimeters runs at room temperature, without the overhead of cryogenics. Nevertheless, these detectors have poor radiation hardness. Sampling cryogenic liquid calorimeters have been used until the current in HEP experiments. For instance, Mark II, R807/ISR, Cello, Helios, NA31, and SLD Experiments by using argon as an active layer (Fabjan & Gianotti, 2003).

2.2.2. Hadronic calorimeter

Because of the strong interactions, an extra difficulty occurs in cascades created by hadrons. These interactions are accountable for:

a. Creation of hadronic cascade particles. The considerable mainstream of the showers (90%) are pions. The neutral pions decay in two photons, which lead to develops electromagnetic showers.
b. Existence of nuclear interactions. In these interactions, protons and neutrons are unconfined from atomic nuclei. The nuclear binding energy of these nucleons has to be provided. Therefore, the fraction of the shower energy required for this function is not included in the calorimeter signals. This phenomenon is called invisible-energy.

Electromagnetic cascades started by pions proceed in a similar way as those originated by high energy photons. The cascade energy segment transmitted by the electromagnetic part (f_{em}) differs from one occasion to another. On average, this fraction rises with the shower energy because pions may be created by higher order shower particles and secondary particles. As the shower energy increases, the further production of shower particles and greater electromagnetic component (f_{em}) occur. Typically, electromagnetic component rises to (50%) at 100 GeV from (30%) at 10 GeV (see Figure 2.5).

In a normal hadron shower evolving in the lead, energy of the non-electromagnetic component is dropped by ionizing particles (56%), invisible energy (34%), and neutrons (10%). The neutrons have typically low energy (3 MeV) on average, for every 1 GeV deposited energy there are 37 neutrons. The protons arise mainly from nuclear decays and they carry naturally 50 to 100 MeV. The above numbers demonstrate that most non-electromagnetic energy is deposited over nucleons instead of pions (relativistic particles).

These characteristics have significant results for a calorimetry:

- Because of invisible energy occurrence, the hadrons calorimeter signals are slighter than for electrons at the same energy.

- The calorimeters are non-linear for the hadrons detection, because the EM energy fraction is energy-dependent.

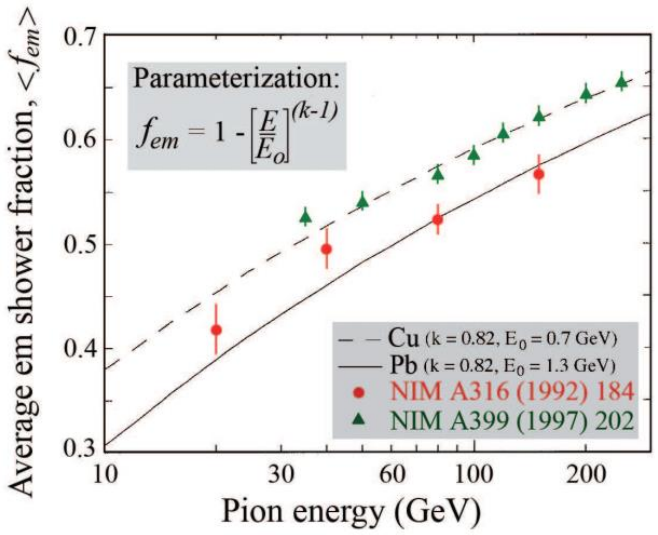

Figure 2.5. Difference between the experimental results on the electromagnetic calorimeter part of pion cascades in lead and copper calorimeters (Wigmans, 2008).

The hadronic cascade profile is controlled by the nuclear interaction length (λ_{int} g/cm^2), i.e., the mean distance hadrons move before producing a nuclear interaction. Hadronic cascade profiles seem vastly comparable to electromagnetic showers demonstrated in Figure 2.2, excluding the scale factor being far prominent in hadronic showers. For example, the radiation length (X_0) for copper reads 1.4 cm, while interaction length (λ_{int}) equals to 15 cm.

Another significant difference between hadronic and electromagnetic showers is seen in the profile changing considerably for the hadronic showers. Figure 2.6 displays four dissimilar cascades produced by pions of 270 GeV energy in lead and iron scintillator calorimeters. The bizarre profiles outcome of the creation of energetic pions in the second or third generation of cascade change. (Wigmans, 2008).

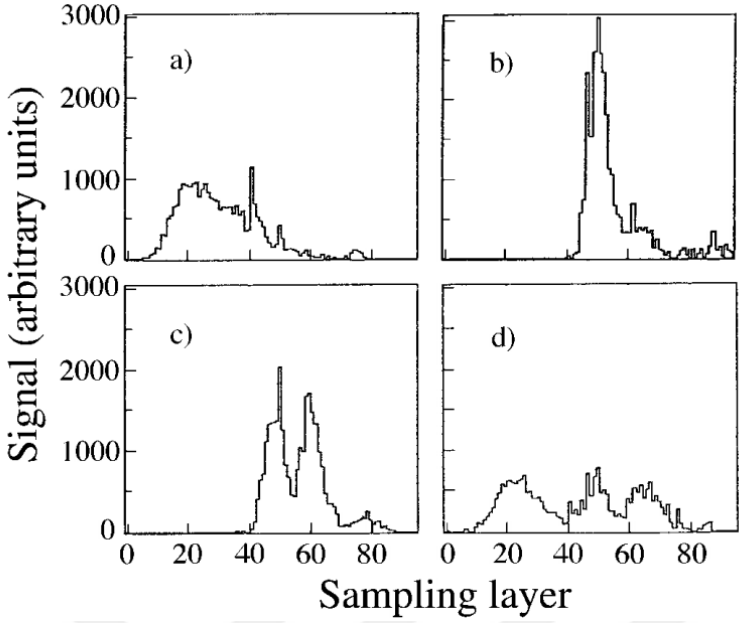

Figure 2.6. Longitudinal shower profiles for four different cascades initiated by 270 GeV pions (Wigmans, 2008).

2.3. Interactions of Charged Particles with Matter

2.3.1. Bremsstrahlung

Charged particles as positrons, electrons lose energy by ionization and interactions with the Coulomb field of the nuclei of the materials. If electrons or photons are slowed in the atomic nuclei's Coulomb field, a portion of their kinetic energy will be released as lights (bremsstrahlung).

The energy loss by bremsstrahlung for high energies can be defined by

$$-\frac{dE}{dx} \approx 4\alpha . N_A . \frac{Z^2}{A} . z \left(\frac{1}{4\pi\varepsilon_0} . \frac{e^2}{mc^2} \right)^2 . E \; ln \frac{183}{Z^{1/3}} \tag{2.8}$$

Where Z stand for the atomic number, A for the atomic weight of the medium, z the charge number, m mass of the incident particle, and E energy of the incident particle.

The bremsstrahlung energy loss of electrons is specified similarly by

$$-\frac{dE}{dx} = 4\alpha . N_A . Z^2 \, z^2 r^2 \, E \, ln \frac{183}{Z^{1/3}} \tag{2.9}$$

Compared to ionization process, in bremsstrahlung process the energy loss is proportional to the incident particle energy and inversely proportional to the square of mass of the incident particles.

For electrons (z=1, m=m_e) Equation (2.8) or Equation (2.9), respectively, can be written in the following manner:

$$-\frac{dE}{dx} = \frac{E}{X_0} \tag{2.10}$$

This equation describes the radiation length X_0 (Grupen & Schwartz, 2008).

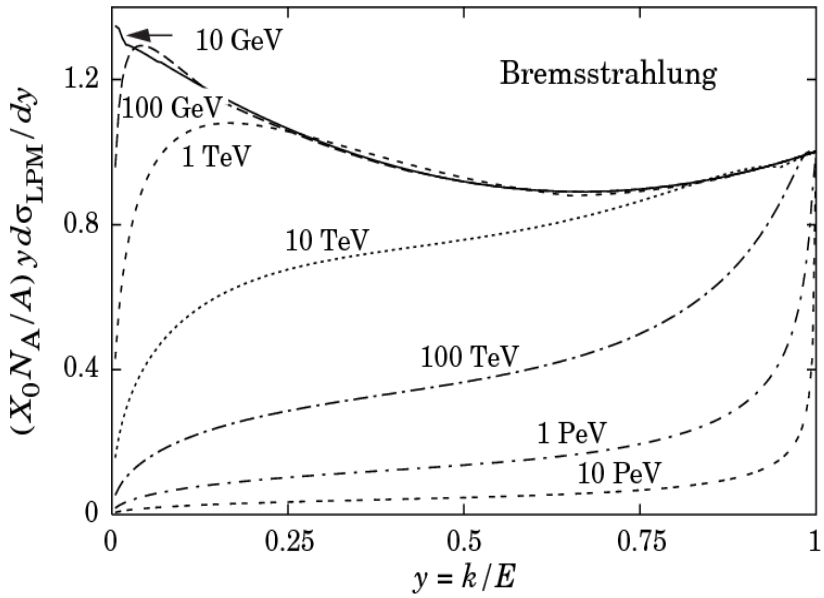

Figure 2.7. Bremsstrahlung cross - section $kd\sigma_{LPM}/dk$ in the lead as a function of the fraction of momentum taken by the radiated photon (Grupen & Schwartz, 2008).

2.3.2. Ionization and excitation

Charged particles such as electrons pass lose kinetic energy through the ionization and excitation of bonded electrons. Excitation can be shown as follows (Grupen & Schwartz, 2008).

$$e^- + atom \rightarrow atom^* + e^- \rightarrow atom + \gamma \tag{2.11}$$

Positrons and electrons primarily lose kinetic energy at low energies by ionization process, though other process like, Bhabha and Møller scattering, and positron annihilation (see Figure 2.8). While the energy loss by ionization increases logarithmically, bremsstrahlung losses growth almost linearly. Ionization loss by positrons and electrons fluctuates from loss by heavy particles as a result of the spin, kinematics, and incident electron's character with the electrons that it ionizes (Desler & Edwards, 2005).

In this case, energy loss dE per length dx is set as

$$-\frac{dE}{dx} = 4\pi\, N_A r_e^2 m_e c^2 z^2 \frac{Z}{A}\frac{1}{\beta^2}\left(ln\frac{2m_e c^2\gamma^2\beta^2}{I} - \beta^2 - \frac{\delta}{2}\right) \tag{2.12}$$

here z: charge of the incident particle, A, Z: atomic weight and atomic number of the medium, m_e : mass of electron, r_e : classical radius of the electron, N_A : Avogadro number, I: average of excitation energy, γ: Lorentz factor, β: relativistic velocity of the particle, and δ: density effect. At particularly high energies excluding bremsstrahlung energy range, the cross section given by

$$\frac{\mathrm{d}\sigma}{\mathrm{dk}} = \left({}^{1}/_{\mathrm{k}}\right)4\alpha \mathrm{r}^2{}_{\mathrm{e}}\frac{N_A}{A}\left\{\left(\frac{4}{3} - \frac{4}{3}\mathrm{y} + \mathrm{y}^2\right)\left[\mathrm{z}^2\left(L_{\mathrm{rad}} - \mathrm{f(Z)}\right) + \mathrm{ZL'_{rad}}\right] + \frac{1}{9}(1-\mathrm{y})(\mathrm{Z}^2+\mathrm{Z})\right\} \tag{2.13}$$

where $y = k/E$ is the element of the electron's energy relocated to the emitted photon, and $A = 1$ g.mol^{-1}, $4\alpha r_e^2 NA/A = (716.408\ \text{g.cm}^{-2})^{-1}$. For example, L_{rad} and L'_{rad} are 5.31 and 6.144 for the hydrogen atom respectively. The function $f(Z)$ is an infinite sum. The perimeter y in the second line of the Eq (2.13) slightly fluctuates between 1.7% to 2.5%. If it is ignored and the first line simplified with radiation length (X_0) provided in Equation (2.1), one can get

$$\frac{d\sigma}{dk} = \frac{A}{X_0 N_A K}\left(\frac{4}{3} - \frac{4}{3}y + y^2\right) \tag{2.14}$$

This cross section (times k) is presented by the top curve in Figure 2.7. By declining energy lesser than 10 GeV, the cross-section declines, and the curves turn out to be rounded as y move to 1. Curves of this familiar shape can be seen in Figure 2.7. But at these excesses, and still, in the complete-screening estimate, the number of photons with energies between k_{min} and k_{max} released by an electron traveling a distance radiation length (X_0) is (Desler & Edwards, 2005).

$$N_\gamma = \frac{d}{X_0}\left[\frac{4}{3}\ln\left(\frac{k_{max}}{k_{min}}\right) - 4\left(\frac{k_{max} - k_{min}}{3E}\right) + \frac{k^2{}_{max} - k^2{}_{min}}{2E^2}\right] \tag{2.15}$$

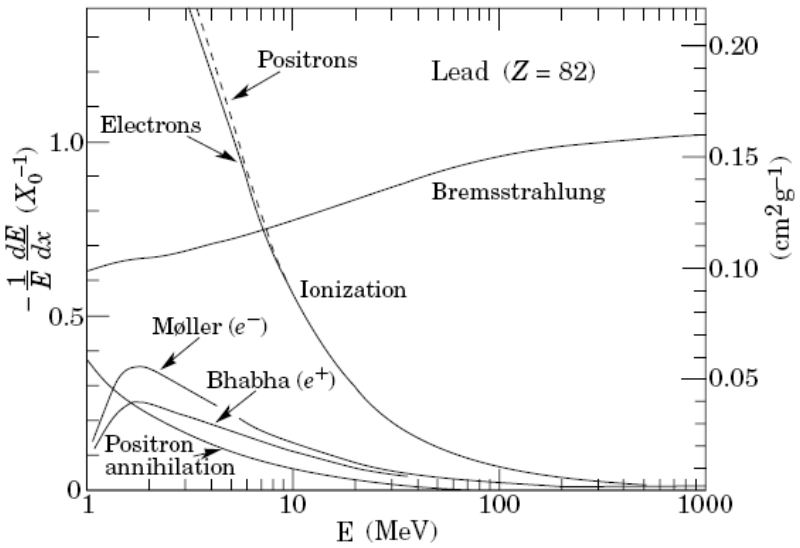

Figure 2.8. Energy loss per radiation length in the lead as a function of positron or electron energy (Fabjan & Gianotti, 2003).

Electrons and positrons scattering are regarded as ionization when the energy loss per collision is less than 0.255 MeV, and as Møller for electrons and Bhabha for positrons scattering when it is greater than 0.255 MeV.

2.4. Interactions of Photons

Photons are identified secondarily through interactions in the detector medium. In this procedure emitted charged particles are verified via their following ionization in the detector's active layer. Photon's interactions are profoundly unlike ionization processes of charged particles owing to the fact that, in all photon interactions, photons are either totally absorbed by the electron-positron pair production process, photoelectric effect, or scattered by the Compton effect by larger angle. For a given photon, any of these three interactions can happen, except the pair production process is occur when energy of the photons is beyond 1.022 MeV. The energy of the photon and the material determine regulate the probability of which interaction potentially arises. Figure 2.9 shows the sections where each kind of photon interaction governs as a function of the energy of the photon and the atomic number of the absorber (Z). the intensity of Photon beams is decreased exponentially in the material as

$$I = I_0 \, e^{-\mu x} \tag{2.16}$$

μ which stands for the mass attenuation coefficient, is linked to cross-sections of different interaction processes of photons and consistent with

$$\mu = \frac{N_A}{A} \sum_i \sigma_i \tag{2.17}$$

Where σ_i stands for atomic cross-section for process i^{th}, A stands for atomic weight, and N_A for the Avogadro number (Grupen & Schwartz 2008).

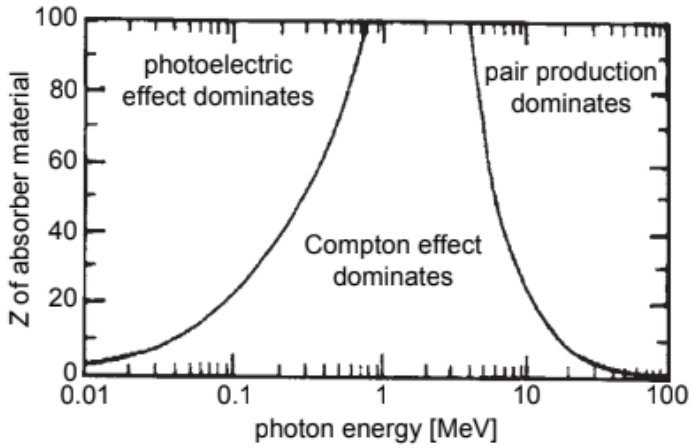

Figure 2.9. Intervals in which interactions dominate as a function of the photon energy and the Z of absorber material (Grupen & Schwartz, 2008).

2.4.1. Photoelectric effect

The mass attenuation coefficient (g/cm^2) changes with the photon energy. For low energies (100 keV ≥ E_γ ≥ ionization energy), the photoelectric effect follows,

$$\gamma + atom \rightarrow atom^+ + e^-. \tag{2.18}$$

Atomic electrons can absorb a photon's energy. Simultaneously, this is not probable for free electrons, because of the momentum conservation law. Photon absorption by an atomic electron involves a third collision partner, which is the nucleus of the atom. The cross-section for the absorption of a photon energy E_γ in the K shell is remarkably prominent due to the proximity of the atomic nucleus. For photoelectric effect, the cross-section in the non-relativistic limit is specified by Born approximation as

$$\sigma^K_{photon} = x\left(\frac{32}{\epsilon^7}\right)^{1/2} \alpha^4 . Z^5 . \sigma^e_{th} \tag{2.19}$$

where the reduced photon energy $\epsilon = {E_\gamma}/{m_e\, c^2}$ and the Thomson cross section is $\sigma^e_{th} = \frac{8}{3}\pi\, r_e^2$ for elastic scattering of photons on electrons.

The cross-section's energy dependence near to the absorption edges is determined by a function $f\ (E_\gamma, E_\gamma^{edge})$. For larger energies, the energy dependency of the cross-section for the photoelectric effect is much fewer articulated,

$$\sigma_{photon}^{K} = 4\pi\ r_e^2\ Z^5\ \alpha^4 \frac{1}{\epsilon} \tag{2.20}$$

Z dependency of the cross-section is estimated by Z^5. This shows that the photon does not interact with a remote electron of the atom (Grupen & Schwartz, 2008).

2.4.2. Compton effect

This effect dominates at the scales of intermediate energies ($E_\gamma \approx 1$ MeV), when photons scattered off by quasi-free electrons of the atom.

$$\gamma\ +\ e^-\ \rightarrow\ \gamma\ +\ e^- \tag{2.21}$$

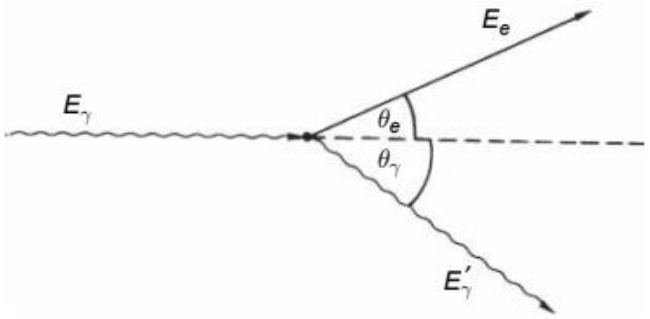

Figure 2.10. Kinematic variables in Compton scattering (Grupen & Schwartz, 2008).

The binding energy of the atomic electrons is neglected in this kind of events. The differential probability of Compton scattering can be provided by Klein–Nishina formula

$$\emptyset_c\left(E_\gamma, E'_\gamma\right)dE'_\gamma = \pi r_e^2 \frac{N_A\ Z}{A} \frac{m_e c^2}{E_\gamma} \frac{dE'_\gamma}{E'_\gamma} \left[1 + \left(\frac{E'_\gamma}{E_\gamma}\right)^2 - \frac{E'_\gamma}{E_\gamma} \sin^2\theta_\gamma\right] \tag{2.22}$$

where θ_γ stands for the scattering angle of incident photon (see Figure 2.10), and E'_γ, E_γ are the energies of the incident and scattered photons. Full cross section in Compton effect per electron can be stated as

$$\sigma_c^e = 2\pi r_c^e \left[\left(\frac{1+\varepsilon}{\varepsilon^2}\right)\left\{\frac{2(1+\varepsilon)}{1+2\varepsilon} - \frac{1}{\varepsilon} ln(1+2\varepsilon)\right\} + \frac{1}{2\varepsilon} ln(1+2\varepsilon) - \frac{1+3\varepsilon}{(1+2\varepsilon)^2}\right] \quad (2.23)$$

Cross section for photons at high energies can be approximately

$$\sigma_c^e \propto \frac{ln\epsilon}{\epsilon} \quad (2.24)$$

The proportion of scattered photon energy to incident photon energy is specified as

$$\frac{E'_\gamma}{E_\gamma} = \frac{1}{1+\varepsilon\left(1-\cos\theta_\gamma\right)} \quad (2.25)$$

The energy transmitted to the electron reaches a highest rate, when

$$\frac{E'_\gamma}{E_\gamma} = \frac{1}{1+2\varepsilon} \quad (2.26)$$

(Grupen & Schwartz, 2008).

2.4.3. Pair production

At higher energies ($E_\gamma \approx 1$ MeV) the pair production happens thorough,

$$\gamma + nucleus \rightarrow e^{+} + e^{-} + nucleus. \quad (2.27)$$

If the photon energy surpasses a particular threshold, the pair production of the electron-positron in the Coulomb field of the atom nucleus is becomes available. In addition to the recoil energy, this threshold energy is specified by the rest masses of two electrons transmitted to the nucleus. From the energy and momentum conservation laws, this threshold energy can be computed by

$$E_{\gamma} \geq 2m_e c^2 + 2\frac{m_e^2}{m_{nucleus}}c^2. \quad (2.28)$$

As $m_{nucleus} \approx m_e$, the actual threshold can be estimated by

$$E_{\gamma} \gtrsim 2m_e c^2. \quad (2.29)$$

Nevertheless, if the electron-positron pair production continues in the Coulomb field of an electron, the threshold energy is

$$E_{\gamma} = 4m_e c^2 \quad (2.30)$$

However, the electron-positron pair production in the Coulomb field of an electron is effectively dominate over those in the columns field of the nucleus. The cross section for electron-positron pair production is given by

$$\sigma_{pair} = 4\pi r_e^2 Z^2 \left(\frac{7}{9} ln 2\epsilon - \frac{109}{54}\right) \quad (2.31)$$

The cross section for total screening of the nuclear charge is

$$\sigma_{pair} = 4\pi r_e^2 Z^2 \left(\frac{7}{9} ln \frac{183}{Z^{1/3}} - \frac{1}{54}\right) \quad (2.32)$$

In low energy regions (E_γ ~ keV) the photoelectric effect is dominants, while in medium energy regions (MeV) Compton scattering is dominant. For high energy photons (at the order of MeV or GeV), the pair production process becomes takes over. For example, in carbon and lead, different processes can occur depending on the energies of the photons. Cumulative cross sections as a function of photon energy in carbon and lead are given in Figure 2.11 (Grupen & Schwartz, 2008).

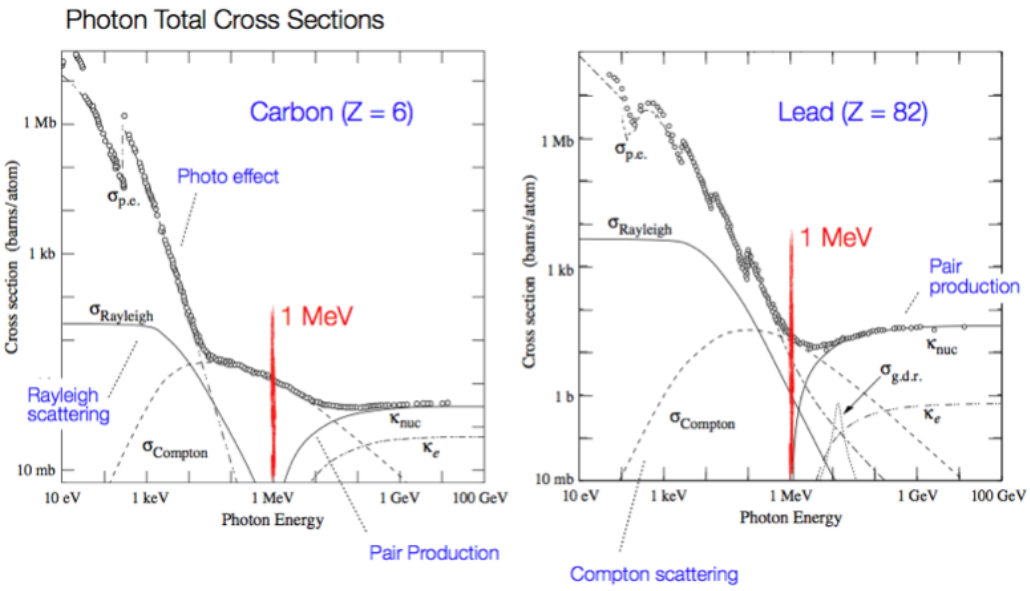

Figure 2.11. Cumulative cross-sections for photon energy in lead and carbon. $\sigma_{compton}$ = Compton scattering off an electron, κ_e = Pair production in electron field, K_{NUC} = Pair production in nuclear field, $\sigma_{p.e}$ = photoelectric effect, $\sigma_{g.d.r}$ = Photonuclear interactions mainly remarkably the Giant Dipole Resonance, $\sigma_{rayleigh}$= Rayleigh scattering–atom neither ionized nor excited (Particle Data Group, 2016).

2.5. Crystals in High Energy Physics Detectors

As a consequence of their efficiency in detection and outstanding energy resolution, for decades, total absorption cascade counters assembled from inorganic scintillation crystals have been experienced in HEP experiments. For nuclear and high-energy physics, significant arrays of crystal scintillators have been manufactured to precisely measure and study photons and electrons and their interactions with matters. The ability of crystal calorimeters was discovered early and established through Crystal Ball's experiment over its research of decays of the Charmonium family and radiative

transitions. Figure 2.12 represents almost all the major lines of radiative flux of the Charmonium system simultaneously estimated by the NaI(Tl) crystal calorimeter.

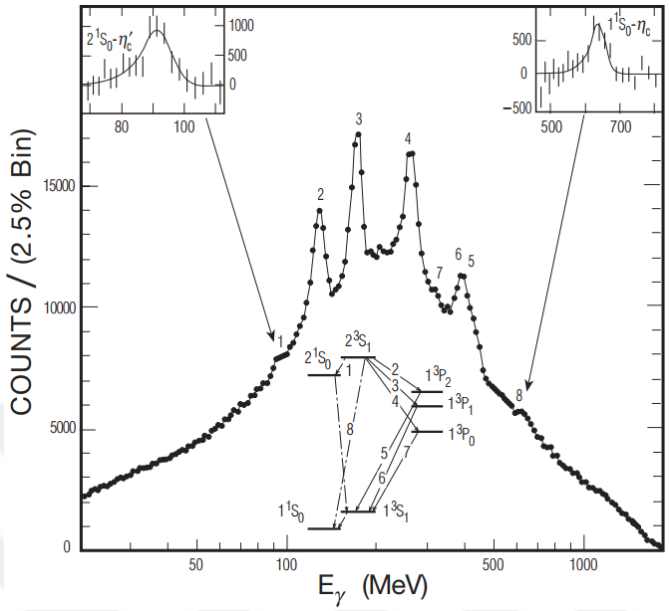

Figure 2.12. A comprehensive photon range calculated at the ψ by the sodium iodide doped with thallium scintillators at SLAC experiments (Zhu, 2006).

The planned purpose of the Compact Muon Solenoid (CMS) detector which is made of ($PbWO_4$) scintillators is to take advantage of its breakthrough ability in investigating for small resonances in electron and photon final states at large hadron collider.

Figure 2.13 illustrates the predictable background-subtracted Higgs peak measured with its decay into a photon pair by $PbWO_4$ crystals at CMS calorimeter. Discovering the Higgs boson through the decay channel was mostly thank to energy resolution of the calorimeters.

The use of calorimeters made of crystal has been a fundamental element in many experimental achievements. With appropriate monitoring and calibration, crystal-based detectors generally accomplish their planned resolution.

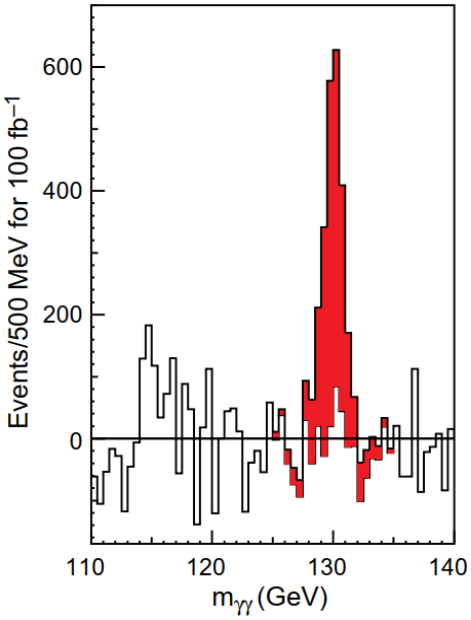

Figure 2.13. The estimated Higgs mass peak reformed from its 2 photon decays measured by the Compact Muon Solenoid lead tungstate calorimeter (Zhu, 2006).

As a function of the incident electron energy, the acquired energy resolution represented in Figure 2.14 which is obtained with an L3 BGO crystal-based calorimeter at CERN, is in excellent compact with the Bhabha electron resolutions calculated at LEP by employing the RFQ calibration (Zhu, 2006).

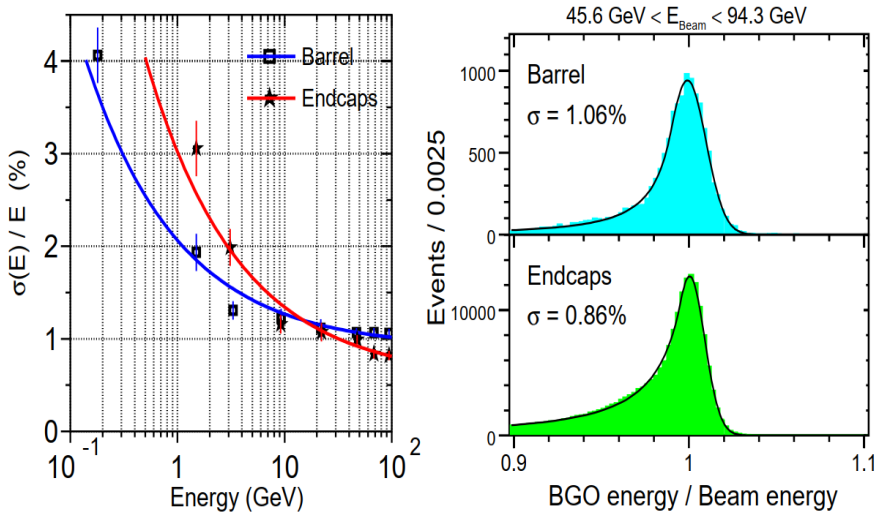

Figure 2.14. The obtained energy resolution for the incident electron for L3 BGO calorimeter measured at CERN (Left). The obtained energy resolution of Bhabha electrons identified by the L3 BGO calorimeter at LEP (Right) (Chaturvedi et al., 2001).

2.5.1. Crystal's detection mechanisms

- Scintillation Mechanism

When a charged particle crosses through a material, it leads to a wake of excited molecules. However, particular kinds of molecules will liberate a small portion of this energy (3%) in form of optical photons. This scintillation is particularly remarkable in organic materials which have aromatic rings, for instance, polyvinyl toluene (PVT) and polystyrene (PS). During this process, the primary excitation appears through photon absorption, and by the radiation of photon having a longer wavelength for de-excitation. Flour is employed as wave shifters to shift light formed from scintillation to a more proper wavelength. Appearing in compound molecules, the emission and absorption processes are extending through a large range of photon energies and have some overlap; that is, there is some portion of the radiated light that can be reabsorbed again (Soo, 2017).

- Cherenkov Mechanism

Cherenkov radiation is specific electromagnetic radiation process when an electron or photon crossing a medium with a velocity v and refractive index n beyond light velocity c/n in that material. This radiation is released since the charged particle polarizes atoms across its path to turn out to be electric dipoles. The emission of electromagnetic radiation is directed by the time variation of the dipole field.

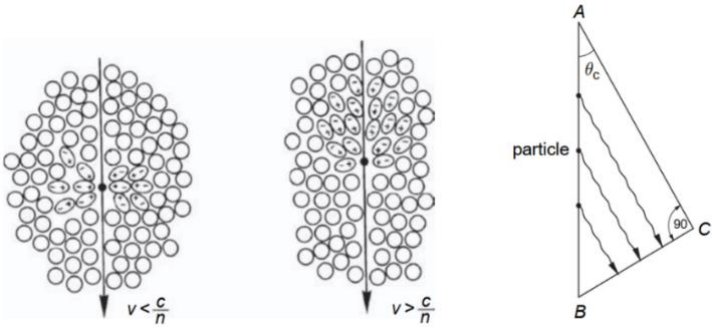

Figure 2.15. Demonstrates the variance in polarization for $v < c/n$ and $v > c/n$, and geometric angle of the Cherenkov radiation (Grupen & Schwartz, 2008).

On the condition that a charged particle velocity (v) is less than light velocity (c/n), the dipoles are equally organized across the particle trajectory, so that the dipole field integrated overall dipoles fall and no radiation arises. Nevertheless, as long as, the charged particle travelling with a velocity (v) greater than light velocity (c/n), the symmetry is broken-down developing in a non- diminishing dipole moment that cause Cherenkov radiation (Grupen & Schwartz, 2008).

The angle between photons released by Cherenkov radiation and the path of the charged particle can be found from (Figure 2.15).

$$\cos\theta_c = \frac{c}{n\beta c} = \frac{1}{n\beta} \tag{2.33}$$

There is a threshold effect for the emission of Cherenkov radiation. This kind of radiation is emitted only if $\beta > \beta c = \frac{1}{n}$. The photons angle rises to makes a highest value when $\beta = 1$, explicitly

$$\theta_c^{max} = \arccos\frac{1}{n} \tag{2.34}$$

The total number of photons produced for wavelengths range from λ_1 to λ_2 are provided with equation

$$\frac{dN}{dx} = 2\pi\alpha z^2 \int_{\lambda_1}^{\lambda_2} \left(1 - \frac{1}{\left(n(\lambda)\right)^2 \beta^2}\right) \frac{d\lambda}{d\lambda^2} \tag{2.35}$$

2.5.2. Inorganic crystal scintilators

When choosing a crystal for a crystal calorimeter in HEP experiments, the selected crystal is characterized by:

- The material characteristics such as melting point, density, machinability, breaking stress, and hygroscopicity.

- Cascade restraint, for instance, Moliere radius R_M and radiation length X_0.
- Scintillation properties like decay speed, temperature dependence, light yield, and light frequency.
- Radiation hardness. (Gratta, Newman & Zhu, 1994).

Table 2.1 listings the main characteristics of heavy crystal scintillators: CsI(Tl), NaI(Tl), CeF_3, BaF_2, lead tungstate ($PbWO_4$), bismuth germanate (BGO), and LSO/LYSO. As revealed in the table, all crystals, excluding CeF_3, have either been actively practiced for or employed in nuclear and high energy physics experiments (Mao, Zhang & Zhu, 2011).

As a function of integration time, calculated via a Photonics XP2254b PMT with multi-alkali photocathode, for five slow crystal (NaI(Tl), CsI(Tl), CsI(Na), BGO and BaF_2), and five fast scintillation crystal (LYSO/LSO, $PbWO_4$, CeF_3 and CsI), light output is demonstrated in Figure 2.16. The BaF_2, $PbWO_4$ scintillators are spotted to contain two decay mechanisms, as indicated in Table 2.1. The LYSO and LSO crystals produce high photoelectron yield, which is 230 and 6 times of $PbWO_4$ and BGO crystals correspondingly and constant fast decay time (40 ns).

Table 2.1. Main properties of heavy crystal scintillators

Crystal	NaI(Tl)	CsI(Tl)	BaF_2	CeF_3	BGO	$PbWO_4$	LSO/LYSO
Density (g/cm^3)	3.67	4.51	4.89	6.16	7.13	8.3	7.40
Melting Point (°C)	651	621	1280	1460	1050	1123	2050
Radiation Length (cm)	2.59	1.86	2.03	1.70	1.12	0.89	1.14
Molière Radius (cm)	4.13	3.57	3.10	2.41	2.23	2.00	1.14
Interaction Length (cm)	42.9	39.3	30.7	23.2	22.7	20.7	20.9
Refractive Index [a]	1.85	1.79	1.50	1.62	2.15	2.20	1.82
Hygroscopicity	Yes	Slight	no	no	no	no	no
Luminescence [b] (nm) (at Peak)	410	560	300 220	340 300	480	425 420	420
Decay Time [b] (ns)	245	1220	650 0.9	30	300	30 10	40
Light Yield [b, c]	100	156	36 4.1	7.3	21	0.30 0.077	85
Experiment	Crystal BALL	CLEO BaBar BELLE BESIII	TAPs		L3 BELLE	CMS ALICE PrimEx Panda	SuperB KLOE

[a] At the wavelength of the maximum emission.

[b] Top line: slow component, bottom line: fast component.

[c] Relative light yield of samples of $1.5X_0$ and with the PMT quantum efficiency taken out.

[d] At room temperature.

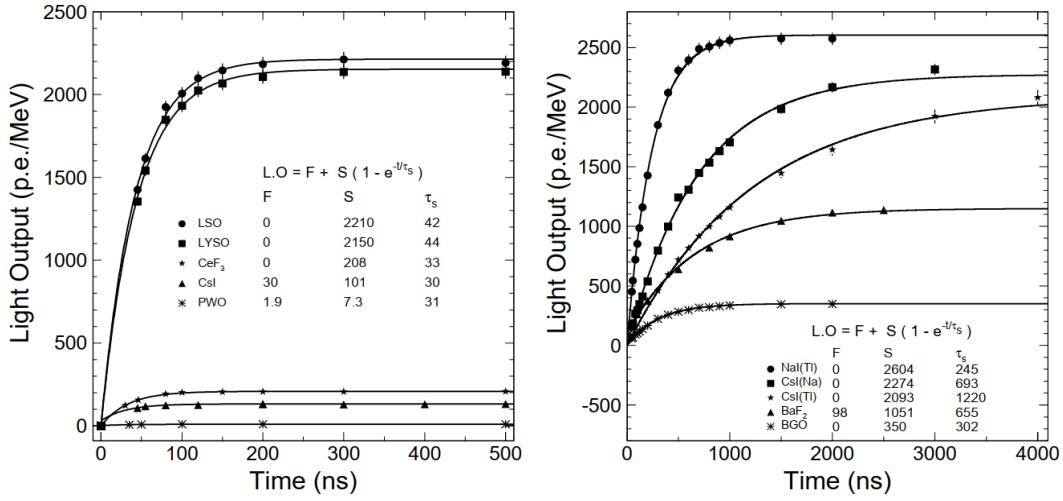

Figure 2.16. Light yield as a function of integration time for 5 quick (Left) and 5 slow (Right) crystal scintillators calculated by XP2254b PMT (Mao et al., 2011).

Figure 2.17 displays an evaluation of the transmittance, emission, and excitation scales as a function of wavelength for eight crystals. The theoretical limit for transmitted photons is shown with solid black square dots. The calculated photons transmittance advances the theoretical limits, showing slight internal absorption. It can be noted that while the BaF_2, BGO, NaI(Tl), CsI(Tl), and $PbWO_4$ crystals control their radiation bands, completely inside the transparent area, the UV absorption edge in the transmittance spectra of the LYSO, LSO, and CeF_3 crystals scintillators cuts into the radiation bands therefore, influences the light output of the crystal. This influence is further very noted for long LYSO and LSO crystals (Mao et al., 2011).

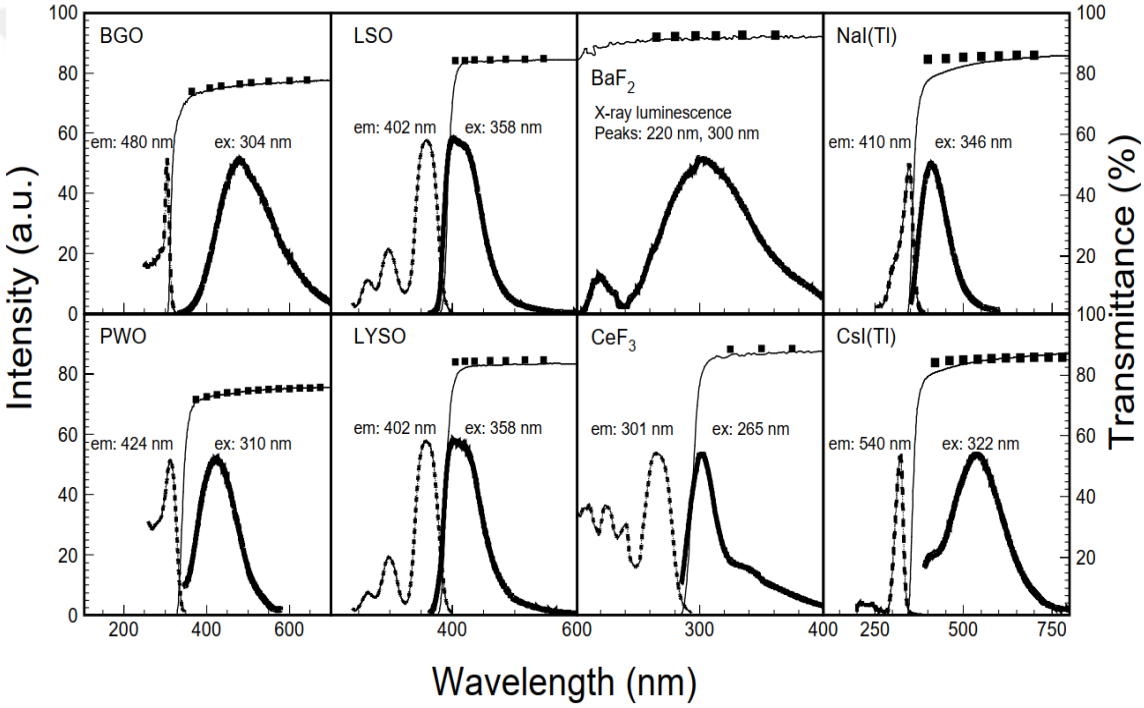

Figure 2.17. Left: the excitation and emission ranges (dashed and thick solid line), right: the transmittance ranges for wavelength spectrum for 8 different crystal scintillators (Mao et al., 2011).

2.6. Position Resolution

Position resolution is characterized as the space between the locations that was reformed by the bunching algorithm and that was reconstructed by the fiber beam define counters (Oishi, 2014). High position resolution measurement, and hence accurate resolution of

photons and electrons angles, are required if the energy resolution of an ECAL is to be completely exploited to deliver exactly restructured invariant masses of resonances decaying to. This was the main problem in the challenging task of the investigating for Higgs mass via its decay channel H→ γ γ.

The location of the collision points of a photon or electron on facade of a calorimeter, or at any other reference plane, can be measured from the prototype of the deposited energies in a bunch of crystals (Gratta et al., 1994).

The most commonly used technique to define the location of particle cascades in a calorimeter is through restructuring the center of gravity ($X_{gravity}$, $Y_{gravity}$) of energy E_i deposited in the different detector units (x_i, y_i) that donate to the signal:

$$X_{gravity} = \frac{\sum_i x_i E_i}{\sum_i E_i} \tag{2.36}$$

Where E_i stands for the deposited energy in the ith row at x-direction, and x_i is the x coordinate of the center of the ith row at the reference plane.

For y coordinates

$$Y_{gravity} = \frac{\sum_i y_i E_i}{\sum_i E_i} \tag{2.37}$$

Where E_i stands for the deposited energy in the ith row at y-direction, and y_i is the y coordinate of the center of the ith row at the reference plane (Wigmans, 2000).

3. MATERIALS and METHOD

3.1. Turkish Accelerator Center (TAC)

TAC scheme is corroborated by the Ministry of Development of Turkey and coordinated by Ankara University (Ankara University, 2020).

The TAC project has four major plans,

- LINAC-ring-class electron-positron collider (Super Charm Factory): TAC project primarily contains a particle factory. This particle factory was projected firstly as a Charm-Tau factory based on a *LINAC* -ring-class electron-positron collider, however, recently, it is altered to a Charm factory based on an ERL-ring class collider having the status of a super factory (Figure 3.1) to increase the luminosity up to 10^{35} $cm^{-2}s^{-1}$.
- Synchrotron radiation facility: The beam current of the synchrotron is designed to be 500 mA with an energy of 3 GeV, and the ring perimeter will be around 546 m.
- Self-amplified spontaneous emission (SASE) free-electron laser (FEL) facility: This scheme was initially on the basis of the collider. However, following many feasibility analyses, it is adjusted to be a standalone facility upon an electron accelerator with an energy of 1 GeV. The purpose of this facility is to visualize the soft X-ray spectrum to a small number of nanometers.
- And a proton accelerator facility: having a beam power of 1 MW a proton accelerator having an energy range of 1 to 3 GeV is designed. Besides, a 3 MeV test stand and a 55 MeV Drift Tube linear accelerator (DTL) will be involved in the character of the low energy section of the sequence (Yavaş, 2012).

After viability and theoretical design studies, the 3rd stage of the scheme began in 2006 as an inter-universities project. The main scientific purpose was to inaugurate an Infrared Free Electron Laser (IR FEL).

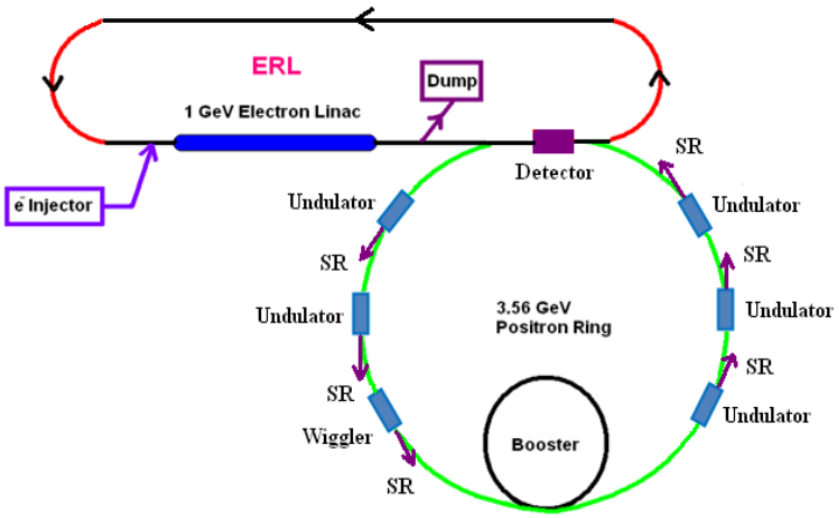

Figure 3.1. Diagram vision of TAC ERL-Ring Super Charm Factory (Aksoy et al., 2014).

Turkish Accelerator Center Particle Factory (TAC-PF) Facility is projected as "super charm factory". It is a ring-form LINAC collider that a 3.6 GeV energy of positron beam from the ring collides with a 1 GeV electron beam from LINAC (Aksoy et al., 2014). The collider is planned with a luminosity of almost 1.4×10^{35} $cm^{-2}s^{-1}$ and the center of mass energy is around 3.8 GeV. Primary factors of TAC-PF Facility can be shown from Table 3.1. The physics goal of the factory is to study from the accuracy assessment of charmed hadrons to the new physics research accompanied by further statistics. A super charm factory will allow the prospect to study charm physics precisely more advance than B factories for similar experimental environments, profiting from a growing factor for particular developments. The detector of the facility will be built for the finding of the generating particles from this collision. The detector is constructed in the region of a 1T superconducting solenoid magnet (SSM) to measure exact momentum for charged particle tracks (Aksu & Piliçer, 2017).

Table 3.1. Primary Factors of TAC-PF Facility.

Parameter	***Positron beam***	***Electron beam***
Energy of the beam (GeV)	3.6	1
Total particles for each bunch (10^{11})	2	0.2
Beta functions at IP β_x/β_y (mm)	80/5	80/5
Normalized emittance $\varepsilon_x^N/\varepsilon_Y^N$	111/0.3	31/0.1
(μm rad)	6	
σ_x/σ_y(μm)	36/0.5	36/0.5
σ_z(mm)	5	5
Number of bunches	300	
Circumference (m)	600	
Luminosity ($cm^{-2}s^{-1}$)	1	$1.4x10^{35}$

3.2. GEANT4 Simulation Program

3.2.1. Overview of GEANT4

GEANT4 is a software toolkit mainly used to simulate the transit of particles across materials. It is employed in many experimentations and developments in a range of application fields, including astrophysics and space science, high energy physics (HEP), radiation protection, and medical physics. GEANT4 modeling potentials and functionality persist to be developed as its performance is improved.

GEANT4 physics developments include various interactions across an expanded range of energy, from high energy interactions at the Large Hadron Collider (LHC) and cosmic ray exploration down to thermal neutrons and optical photons interactions. Particles traced by GEANT4 involve photons, leptons, ions, and hadrons. Different applications of physics activities are presented, offering alternative or complementary modeling methods. Furthermore, this toolkit offers interfaces to allow its users to communicate with their usage and memorize their findings. Graphical user interfaces,

visualization drivers and interfaces, and a resilient framework for persistency are involved in the package.

The foundation of GEANT4 simulation can be attributed to two pieces of researches performed autonomously in 1993 at CERN and KEK. These two collaborations study the ability of contemporary computing methods could be used to progress what was presented by the existing GEANT3 simulation, which was a standard and foundation of concepts and treasured knowledge. Both accomplishments compound and submitted to the CERN Detector Research and Development Committee (DRDC) to build a simulation program upon object-oriented technology. RD44 was the resulting project that adapting an object-oriented methodology based on the C++ language.

GEANT4 program is motivated by the software requirements of contemporary experimentations. A characteristic software system includes event generator or components, detector simulation, analysis and reconstruction that can be operated in combinations or individually (Agostinelli et al., 2003).

3.2.2. General structure of GEANT4

GEANT4 involves 17 class categories, explained in Figure 3.2, separately is autonomously advanced and maintained by a working group.

The GEANT4 kernel involves categories that offer central functionality of the toolkit: manages events, runs, steps, tracks, trajectories, hits, applies GEANT4 as a state machine and delivers a background for: physics processes, visualization drivers, persistency, histogram / analysis and user code. From the graph, we perceive that the Global category is the first to be exercised. This category is regulating the system of units, constants, numeric, and random number treatment. The Graphical Representations category and the Intercoms category both exploit Global. The Intercoms principally operate as a manager between the operator and GEANT4 via the user interface. Graphical Illustrations play a role in the volumes for detector explanation and navigation in the geometry prototype.

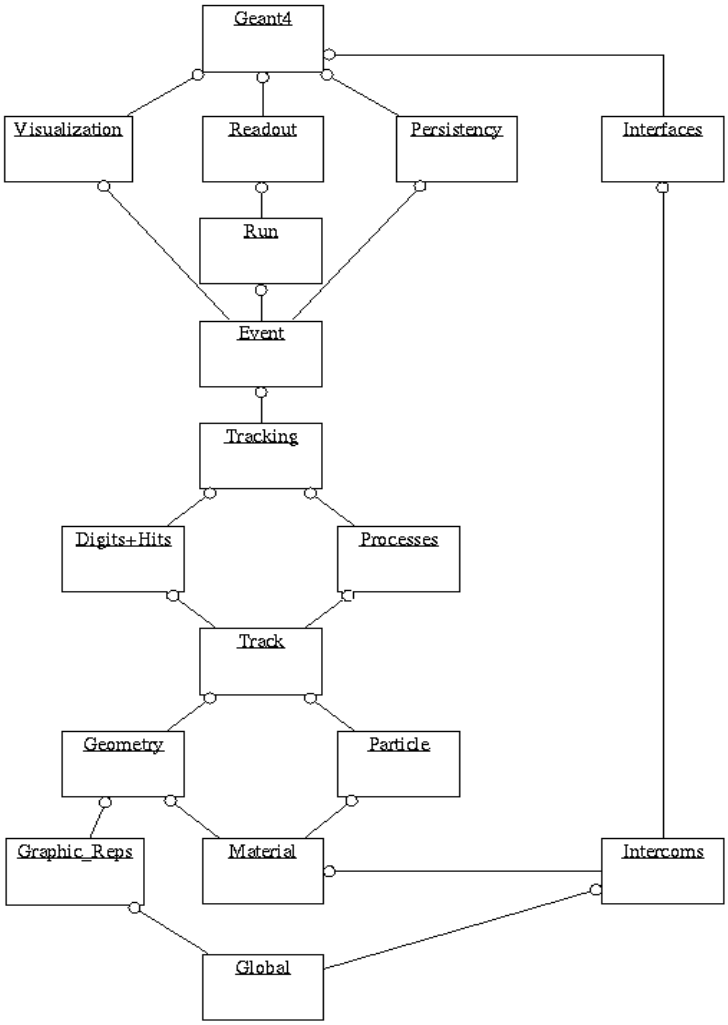

Figure 3.2. Class category diagram of GEANT4 (Agostinell et al., 2003).

Information is then spread through to the Substance, Particle, and Geometry categories. The first two employ facilities essential to define the physical characteristic of materials and particles for the simulation of interactions between matter and particle (Agostinell et al., 2003). The last of which presents the facility to designate a geometrical configuration and transmit particles effectively across it (Brun, Hagelberg, Hansroul & Lassalle, 1978). At this point, we get the categories that are accountable for explaining our events. The first category to act a role in this is the Track category, which includes classes accountable for the tracks and steps. It is exploited by the Method classification, which covers applications of physical interaction models: electromagnetic interactions of photons, leptons, ions, and hadrons, and hadronic interactions. At this point, all the categories mentioned so far are occupied either directly or indirectly for Tracking, the

category that controls their role to the development of a track's state and undertakes to delivers information in sensitive dimensions for hits and digitization. At this point, the Event class controls event tracks, and the Run administers a collection of events that allocate a joint beam and detector application. At this point, Event delivers the data to the Readout through Run and forwards data to the Visualization and Persistency categories (GEANT4 Collaboration, 2020).

3.2.3. GEANT4 simulation units

Several simulation units are used in GEANT4 and must be introduced to the user before starting to build an application.

- A run: The main unit of simulation in GEANT4 is a run. The class G4Run characterizes it. A run is a group of events that are formed under identical conditions. Within a run, the user cannot modify the detector or system geometry, nor the Physics process settings. By correspondence to high energy physics, a GEANT4 run starts with the command "beamOn." The detector is unapproachable once the beam is on. At the start of a run, the geometry is optimized for navigation, and cross-sections are computed according to materials in the setup, low-energy cutoff values are defined.
- An event: At the start of processing, an event covers primary particles (from a particle gun, a generator, etc.), driven onto a stack. Throughout the processing, each particle is exploded from the stack and traced. When the stack is vacant, the event processing is finished. The class G4Event describes an event. At the end of handling, it has the next objects: list of primary particles and vertices (the input), digitization collections, hits collections, trajectory collections.
- A track: Is a shot of a particle inside its background when the particle passages. The measures of snapshot alter at every individual occasion; a track has a physical magnitudes and position it is not a group of steps. A tracked object (class G4Track) has a lifetime, it is shaped by a physics method such as decay or a generator, and it is erased when it exits the World mother volume, disappears, reaches zero energy, and no “at rest” activity is characterized, or the user kills it.
- A step: (class G4Step) Is the key component of simulation; it has pre- and post-step points (Figure 3.3) and it includes the incremental particle data like elapsed time and

energy loss. Every point comprises data for material and volume. If a boundary restricts the step, the endpoint stands precisely on the edge, however, are reasonable element of the next volume. For this reason, boundary processes, for instance, radiation caused by transition and refraction can be simulated (Sébastien, 2020).

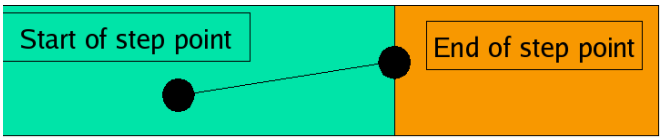

Figure 3.3. Step definition (Sébastien, 2020).

3.3. TR- Grid (TRUBA) System

Grid is a structure that allows researchers to have a single computer system structure with middleware software instead of accessing resources spread around the world separately and manually.

Grid computing techniques and infrastructure are primarily used by universities and research institutes for academic studies. In this context, the main working areas are;

- High Energy Physics
- Basic Sciences (Physics, Chemistry, Mathematics)
- Biomedical
- Earth Sciences
- Weather Prediction Research
- Space Sciences
- Brain Dynamics Research
- Computer Science
- Materials Science
- Genetic Research (Onur, 2005).

Calculations made with the GEANT4 program in this thesis were conducted by TUBITAK ULAKBIM High Performance and Grid Computing Center which, is a nationwide center supplying data storage and extraordinary performance computation for all research organizations and researchers in Turkey.

TR-Grid is a 128-processor cluster initiative founded in 2003 with the partnership of, İstanbul Technical, Bilkent, and Boğaziçi universities.

TR-Grid initiative primary purposes are:

- build up the national grid infrastructure,
- transfer information to national user society regarding grid infrastructure and international grid projects and high-performance computing as well,
- actively take place in international grid projects,
- develop high-performance computing resources with an association of commercial members and academic researchers,
- expand national applications (Cem, 2005).

Since 2003, TUBITAK ULAKBIM High Performance and Grid Computing Center is a state foundation aiming to provide a computing environment for research groups across the country. This center also continued its activities as the founder and coordinator of the National Grid Formation (TR-Grid UGO). Since 2010, the name of the infrastructure has been changed to Turkish National Science e-Infrastructure (TRUBA). TRUBA Formation provides services by being set up together with the services and tools required by national high-performance grid and cloud computing infrastructures. With its experienced staff and sustainable infrastructure, it continues to work as a partner in international, regional and national projects.

The general objectives of the TRUBA Formation can be listed as follows:

- Operating and expanding high-performance grid and cloud computing and storage infrastructure.
- To create a national e-Infrastructure created with standards and road maps throughout the country by expanding the scope of working models created with different centers and research groups in TRUBA.
- To ensure the integration of TRUBA to new technological developments in e-Infrastructures.

The resources in the TUBITAK ULAKBIM High Performance and Grid Computing Center, which inaugurated its functions in 2003, are integrated with TRUBA. Currently, provides Turkish academics with around 15,000 processor cores, 36 graphics processing units, (GPU) and a total of 2PB Luster file system (TRUBA Wiki Sayfası, 2020).

4. RESULTS and DISCUSSION

Monte Carlo-based GEANT4 simulation code (Agostinelli et al., 2003) was used to execute the simulation development for 0.1 GeV to 2 GeV electrons spreading across the electromagnetic calorimeter part made up of 3×3 LYSO crystals. The incident electrons were pointed vertically at a 0-degree angle at first place and at different angles to the module as can be seen in Figure 4.1. The simulation process was accomplished by using *GEANT4.10.04-patch-03* with the *QGSP-BERT 4.5* physics list. The LYSO crystals have 25×25 mm^2 in cross section ($1.2R_M$) with 200 mm length ($17.5X_0$).

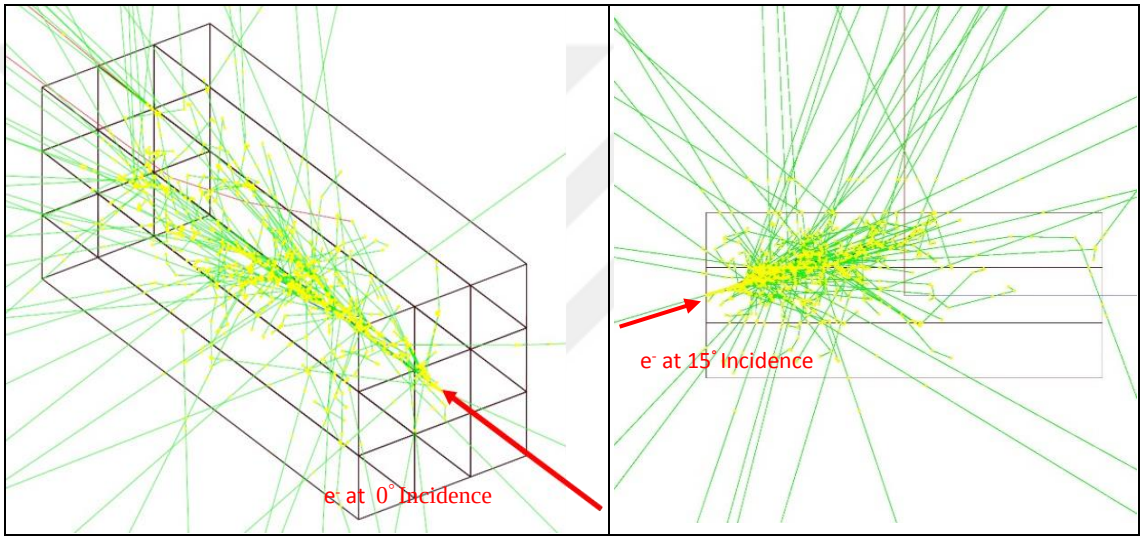

Figure 4.1. 3×3 LYSO crystal matrix.

In this simulation process, in order to acquire the allocations of gravity center of electron energies deposition in the matrix, electrons were sent at 14 different points to the front face of the central crystal of the LYSO matrix at various energies. Using equations 2.36 and eq. 2.37, the position of electron can be calculated. The correlation among $x_{gravity}$ and $y_{gravity}$ in the center of the LYSO matrix for 2 GeV, 1.5 GeV, 1 GeV, and 0.5 GeV electrons can be seen in Figure 4.2.

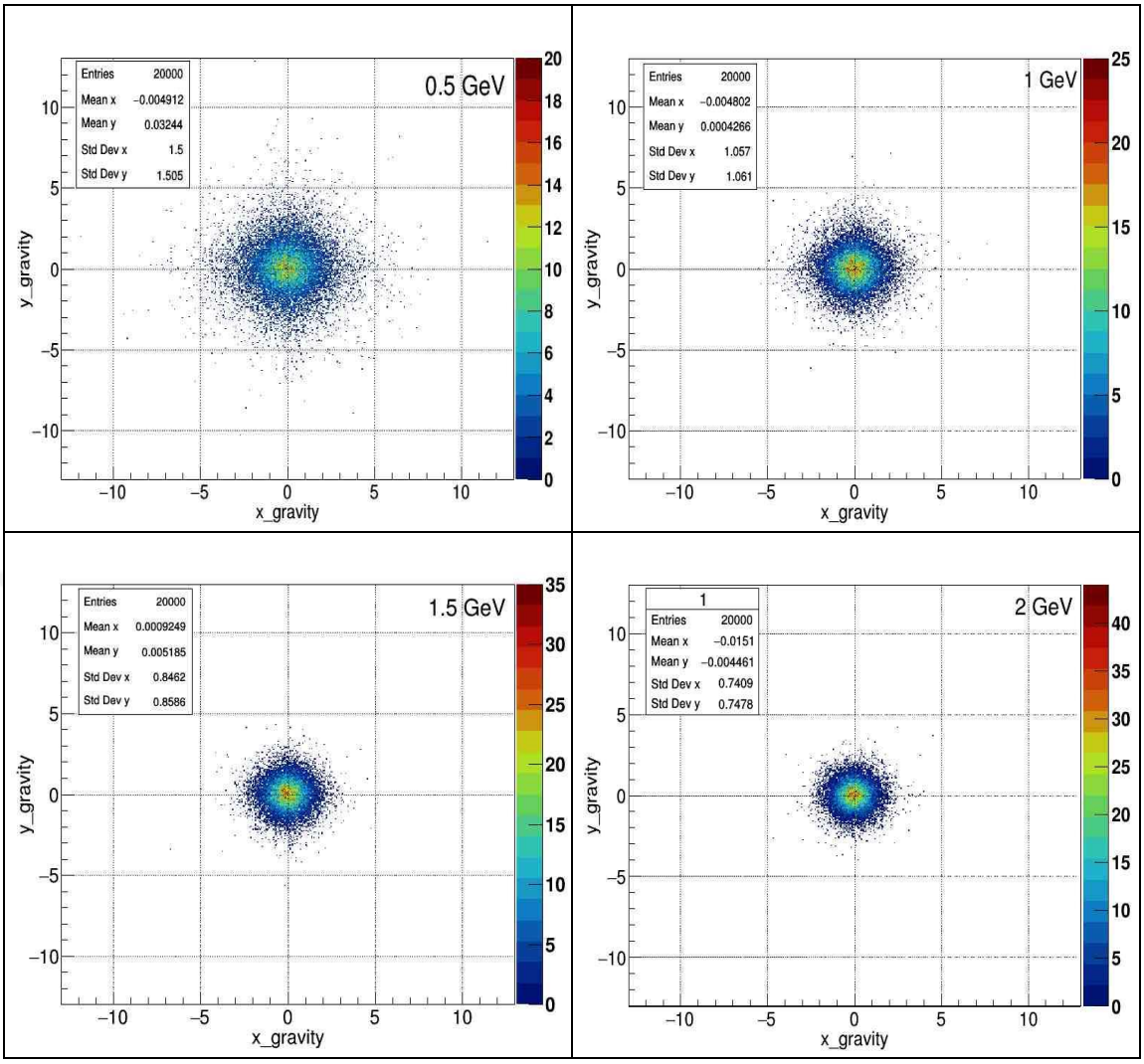

Figure 4.2. Relation between $x_{gravity}$ and $y_{gravity}$ in the center of LYSO matrix for 0.5, 1, 1.5, and 2 GeV electrons.

The correlations between calculated positions ($x_{gravity}$ and $y_{gravity}$) versus the true positions (x_{true} and y_{true}) in which the electron has been injected, are shown in Figure 4.3 for 0.5 GeV, 1 GeV, 1.5 GeV, and 2 GeV electrons (S-shape). The weighted sum method results in biases this S-shapes calculation towards the center of the LYSO crystal matrix as seen in this Figure 4.3 and 4.5 (Batarin et al., 2003).

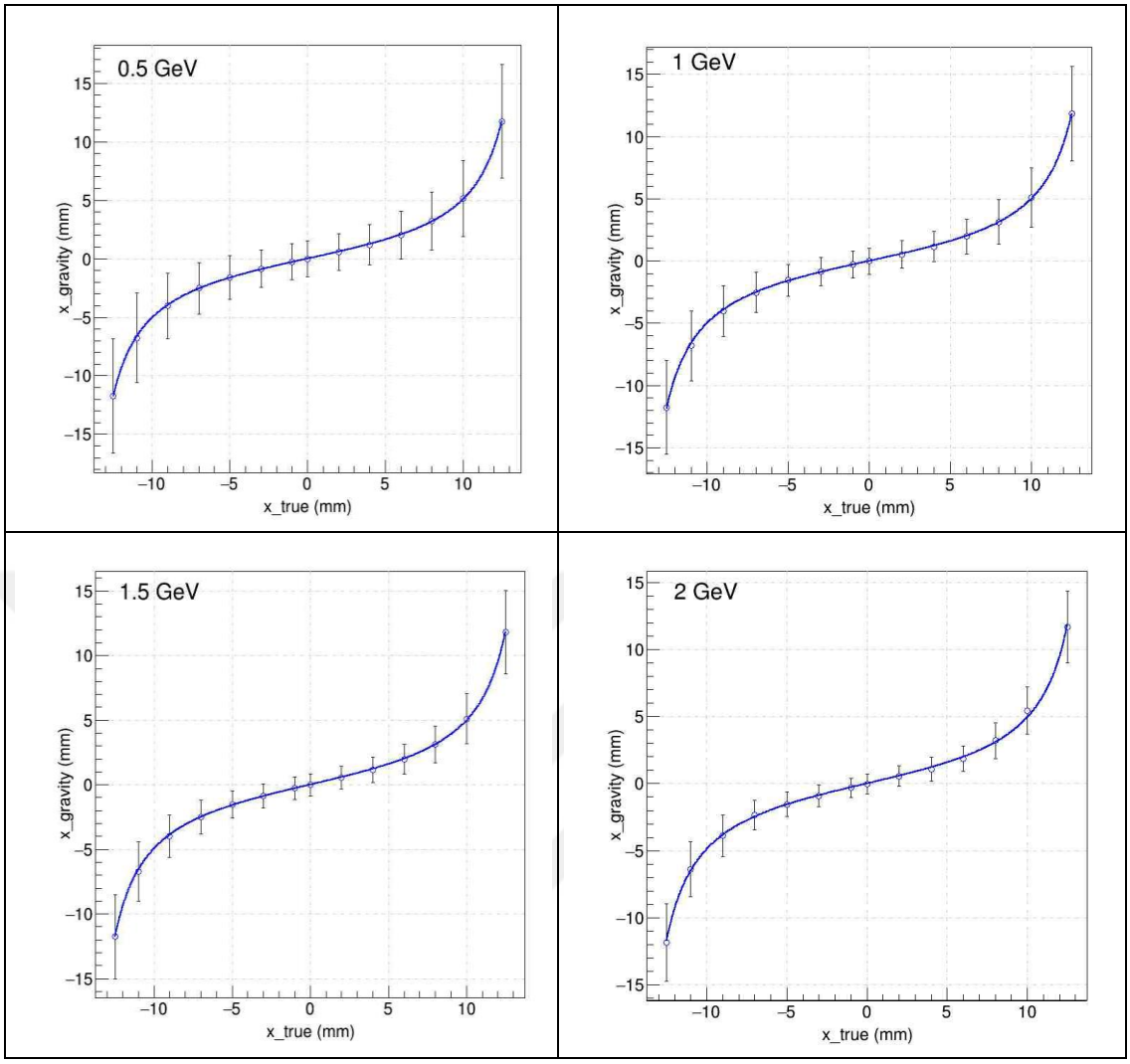

Figure 4.3. Position obtained by $x_{gravity}$ vs. x_{true} for 0.5, 1, 1.5, and 2 GeV electrons. The S-curve represented with solid blue line.

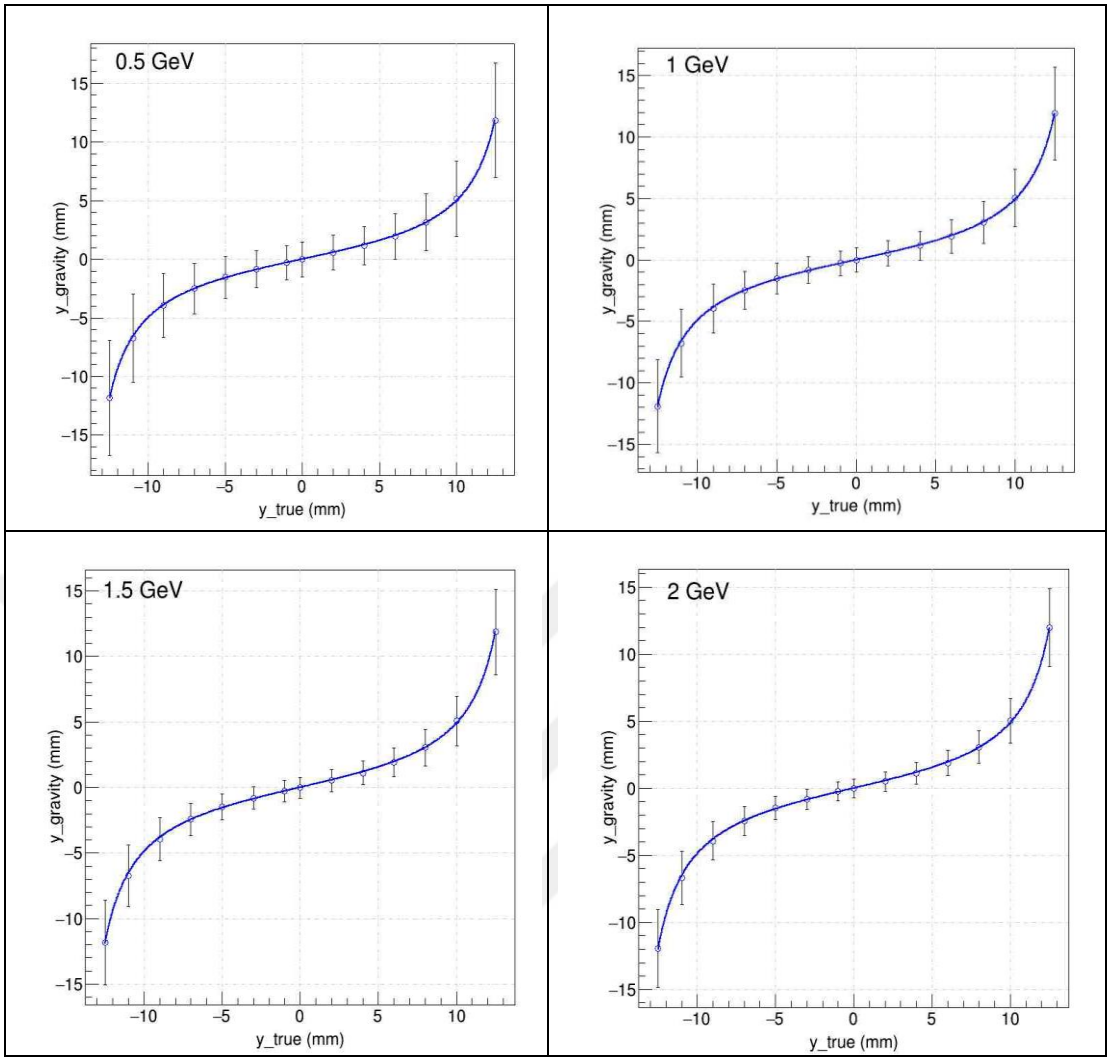

Figure 4.4. Position obtained by $y_{gravity}$ vs. y_{true} position for 0.5, 1, 1.5, and 2 GeV electrons. The S-curve represented with solid blue line.

If the impact point of the incident electron is in the center of matrix or close to the edge between the separate crystals, the position of the electron can be properly restructured, as shown in Figure 4.3 and Figure 4.4. In all other circumstances, the majority of electron energies in the cascade is deposited in the affected crystal and there is an exponential reduction in the shared energies between adjacent crystals.

To remove the nonlinearity dependency (as can be shown appear in S-curve) between the calculated positions *($x_{gravity}$* and *$y_{gravity}$)* and impact positions *(x_{true}* and *y_{true}),* the S-shape fit equation was employed. This is an empirical algorithm and given as

$$x_{gravity} = c \ \tan d \ (x_{true} - e) \quad (4.1)$$

Where $x_{gravity}$ and x_{true} are given in mm. By means of the fit process, for instance, the parameters c, d, and e, at 1 GeV are found to have the values of 2.67, 0.11 and 0.001 respectively. And similarly in Y coordinate given as

$$y_{gravity} = c \ \tan d \ (y_{true} - e) \quad (4.2)$$

Here $y_{gravity}$ and y_{true} are also given in mm as well. The parameters c, d, and e at 1 GeV are obtained as 2.577, 0.108 and 0.001, respectively, similar to the values obtained on the x-axis. Table 4.1 and 4.2 exhibits the attained fit findings for the incident electron with energies range from 0.1 to 2 GeV in the x-axis direction and y-axis direction respectively.

Table 4.1. Calculation results of the c, d and e parameters of the position resolution for 3×3 LYSO matrix for different energies in x coordinates.

Electron's energy (GeV)	**c (mm)**	**d (rad/mm)**	**e (mm)**
0.1	2.166	0.112	-0.007
0.25	2.327	0.110	0.017
0.5	2.739	0.107	-0.003
0.75	2.702	0.108	-0.004
1	2.669	0.108	0.0001
1.25	2.63	0.108	-0.023
1.5	2.651	0.108	-0.003
1.75	2.654	0.108	0.003
2	2.613	0.108	-0.01

Table 4.2. Calculation results of the c, d and e parameters of the position resolution for 3×3 LYSO matrix for different energies in y coordinates.

Electron's energy (GeV)	c (mm)	d (rad/mm)	e (mm)
0.1	2.175	0.112	0.014
0.25	2.365	0.110	-0.003
0.5	2.663	0.108	-0.004
0.75	2.616	0.108	0.002
1	2.598	0.108	0.006
1.25	2.583	0.109	0.003
1.5	2.577	0.109	0.001
1.75	2.567	0.109	0.005
2	2.548	0.109	0.002

As can be seen in above tables, since the Moliere radius is loosely reliant on energy, the parameters vary slightly with the deposited energy of electron. For the purpose of calculating the corrected position in the x-axis ($x_{corrected}$), the parameter values of c, d, and e that are found from the fit, have been employed in the following equation.

$$x_{corrected} = \frac{1}{d}\tan^{-1}\frac{x_{gravity}}{c} + e \tag{4.3}$$

To obtain the corrected position in the y-axis ($y_{corrected}$), the related computations also were made using the following equation, similar to the one in the x-axis.

$$y_{corrected} = \frac{1}{d}\tan^{-1}\frac{y_{gravity}}{c} + e \tag{4.4}$$

The obtained corrected position distributions have almost a gaussian form (see Figure 4.5). The corrected position distributions have been fitted by employing the gaussian function to acquire the position resolution for the LYSO matrix. The sigma values of these spectra shown in Figure 4.5, give the simulated position resolutions for the crystal

calorimeter for electron energy of 0.5 GeV, 1 GeV, 1.5 GeV, and 2 GeV in the X and Y directions respectively.

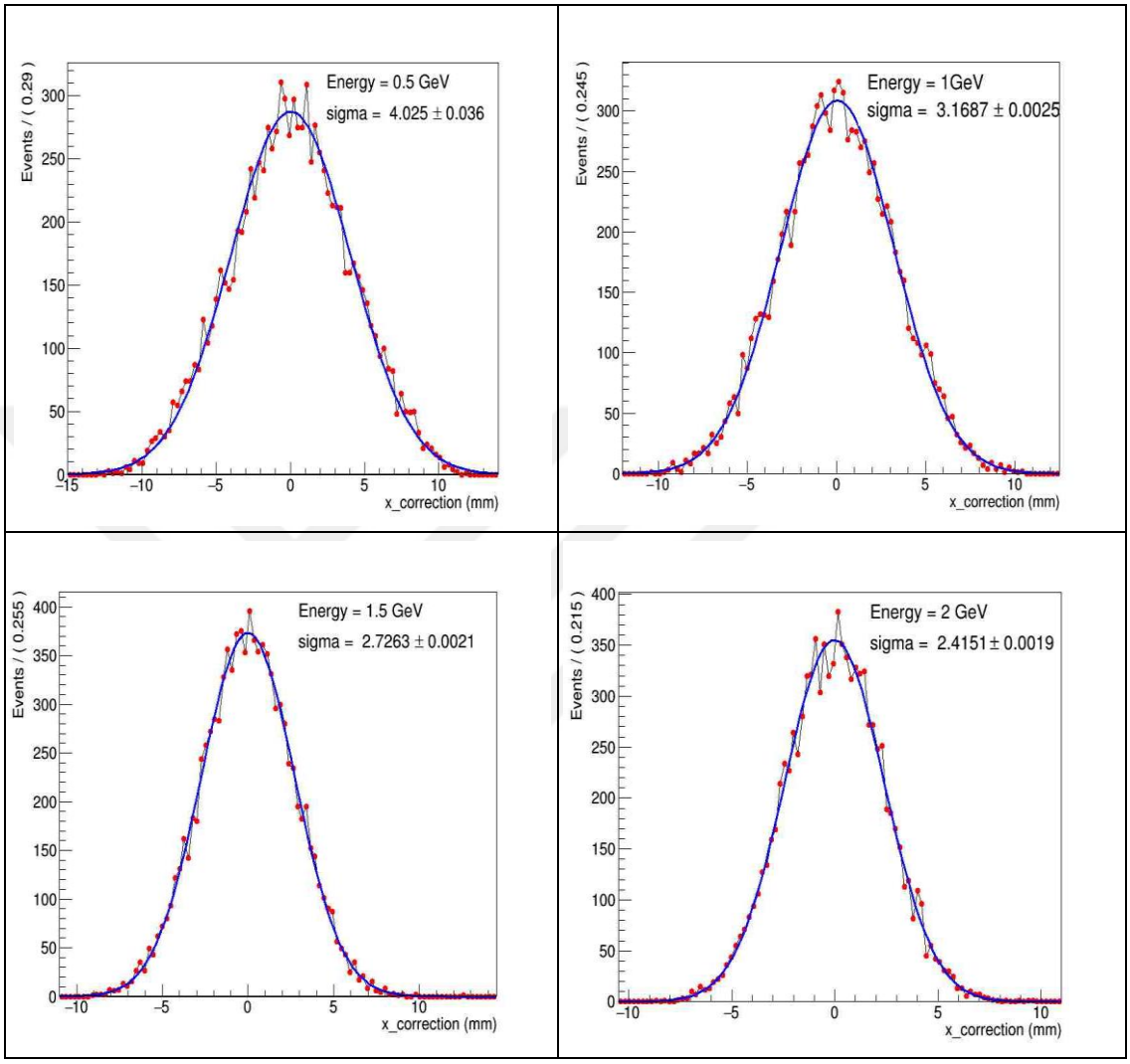

Figure 4.5. S-shape correction $x_{corrected}$, for electron having energy of 500 MeV, 1 GeV, 1.5 GeV, and 2 GeV.

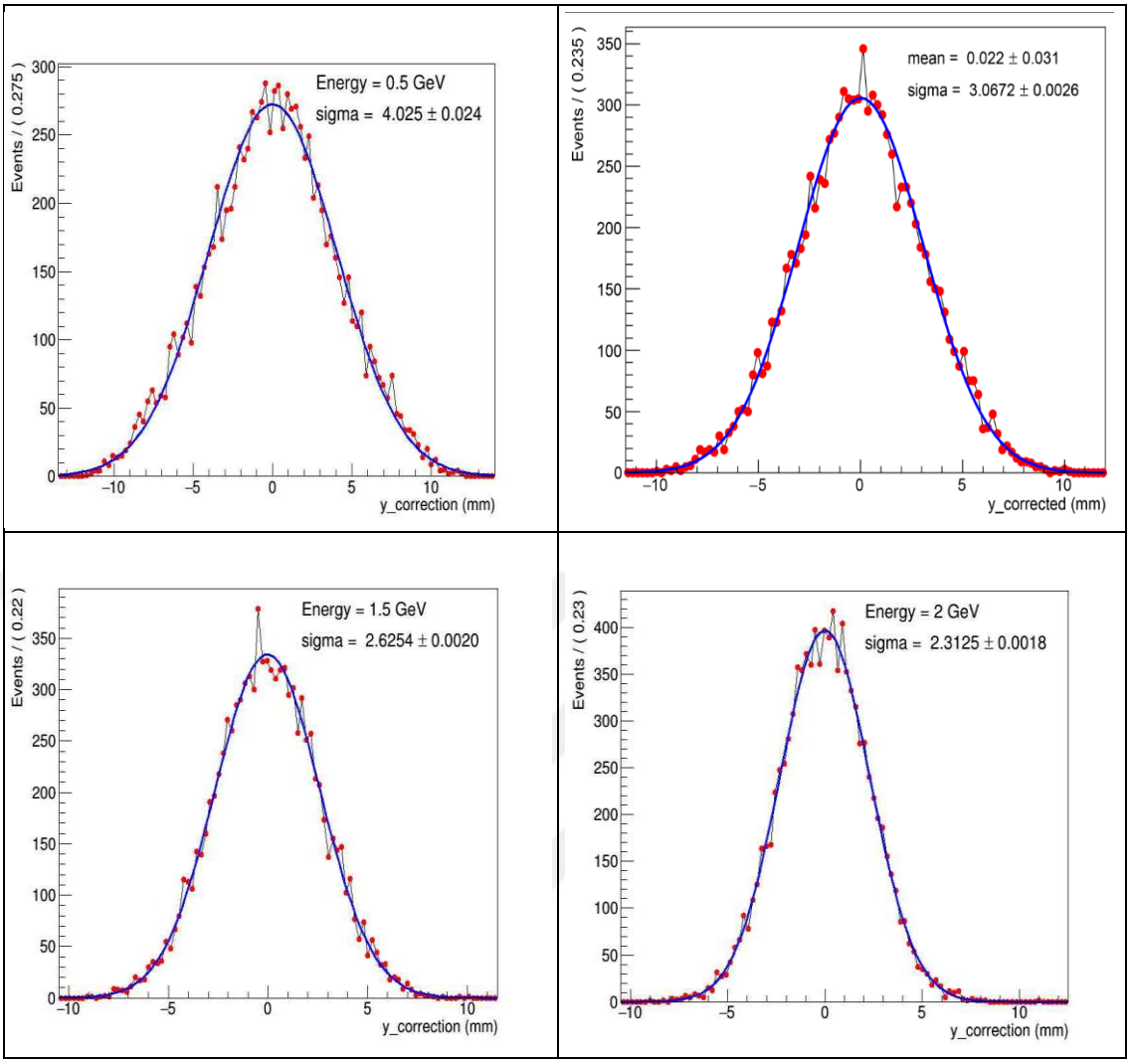

Figure 4.6. S-shape correction $y_{corrected}$, for electron having energy of 500 MeV, 1 GeV, 1.5 GeV, and 2 GeV.

Figure 4.7 displays the corrected position ($x_{corrected}$) as a function of true position (x_{true}) for electron with energies of 0.5 GeV, 1 GeV, 1.5 GeV, and 2 GeV in the x directions. And Figure 4.8 displays the corrected position ($y_{corrected}$) as versus the true position (y_{true}) for similar electron energies.

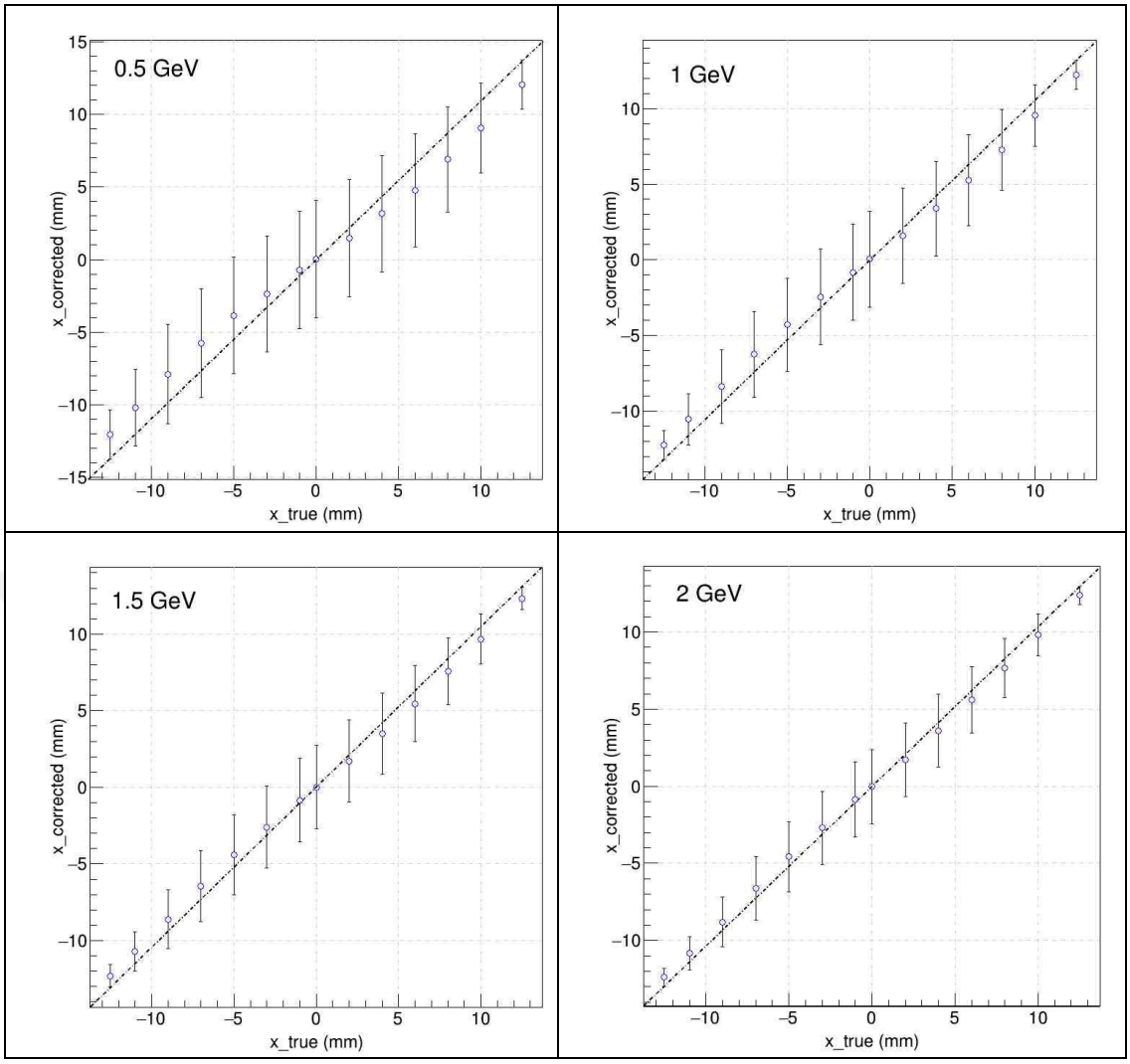

Figure 4.7. Dependency of the corrected position ($x_{corrected}$) in LYSO scintillators on the impact position (x_{true}).

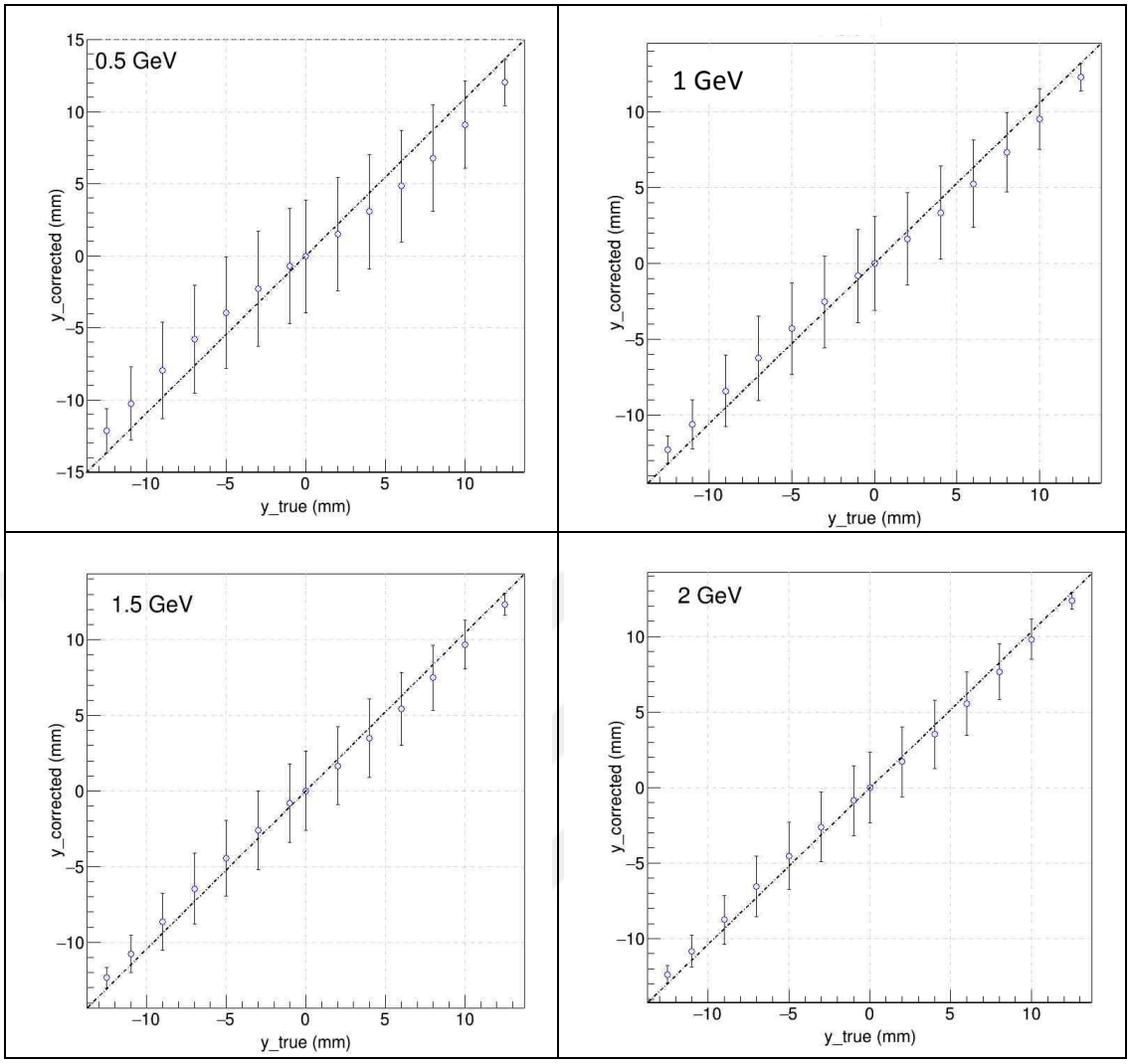

Figure 4.8. Dependency of the corrected position ($y_{corrected}$) in LYSO scintillators on the impact position (y_{true}).

Figure 4.9 and Figure 4.10 show the obtained position resolutions in x and y directions at different positions in LYSO crystal for electrons with energies range between 0.1 and 2 GeV. Results simulated with GEANT4 show that the simulated position resolution enhances when the energies of the incident electrons rise.

In order to obtain the dependence of position resolution on the incident particle energy, the following equation can be used:

$$\sigma(mm) = \frac{a}{\sqrt{E}} \oplus b \tag{4.5}$$

At the central LYSO crystal (at coordinate x= y= 0), the position resolutions subject to the energies of the incident electrons can be calculated as

$$\sigma_x(mm) = \frac{(2.77 \pm 0.07)}{\sqrt{E}} \oplus (1.46 \pm 0.10) \tag{4.6}$$

for the x coordinate, and

$$\sigma_y(mm) = \frac{(2.77 \pm 0.05)}{\sqrt{E}} \oplus (1.31 \pm 0.07) \tag{4.7}$$

For the y coordinate. The variation of the fit parameters *a* and *b* of the position resolution for various impact position of electrons on the x and y axis can be seen in Table 4.3 and Table 4.4.

The position resolution is changes on the basis of the incident electron impact position and has better values towards the edge of the crystal, as seen in Figure 4.9 and Figure 4.10. This is due to the fact that the electromagnetic shower sharing between nearby crystals starts to turn out to be significant in that position of the crystal.

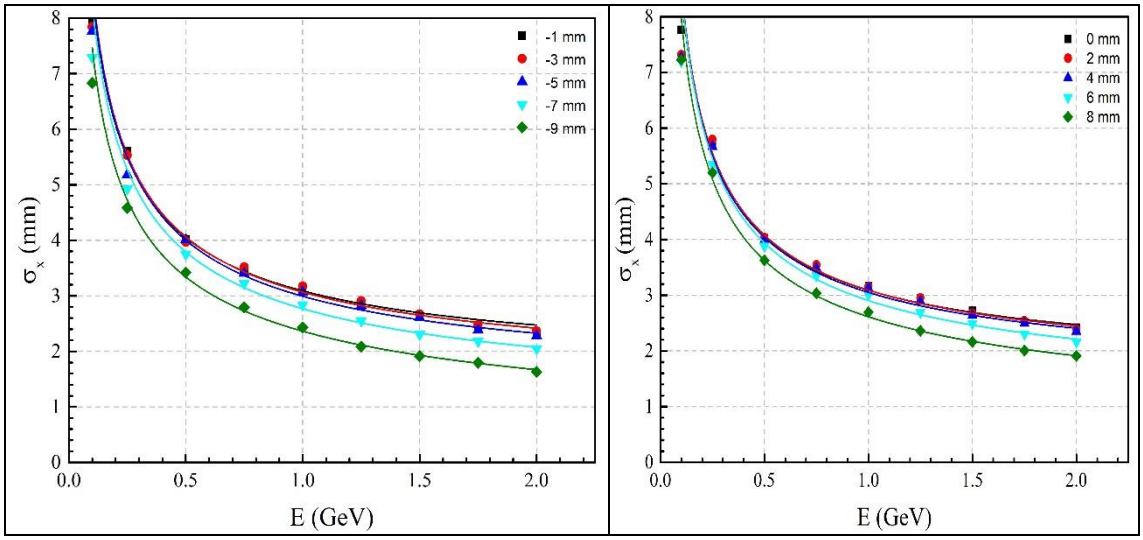

Figure 4.9. Obtained position resolutions in x coordinates at the central crystal of the 3×3 LYSO matrix as a function of electron energies. The lines are the fits of the data. The error bars are smaller than the symbols presented.

Table 4.3. The fit parameters of position resolution for different incidence positions of electrons in x coordinates.

Impact Position [mm]	*a*	*b*
8	2.52 ± 0.08	0.71 ± 0.20
6	2.66 ± 0.12	1.16 ± 0.20
4	2.65 ± 0.13	1.52 ± 0.17
2	2.66 ± 0.14	1.57 ± 0.18
0	2.77 ± 0.07	1.46 ± 0.10
-1	2.28 ± 0.08	2.07 ± 0.17
-3	2.21 ± 0.07	2.09 ± 0.15
-5	2.08 ± 0.11	2.12 ± 0.22
-7	2.02 ± 0.12	1.84 ± 0.25
-9	1.96 ± 0.10	1.25 ± 0.26

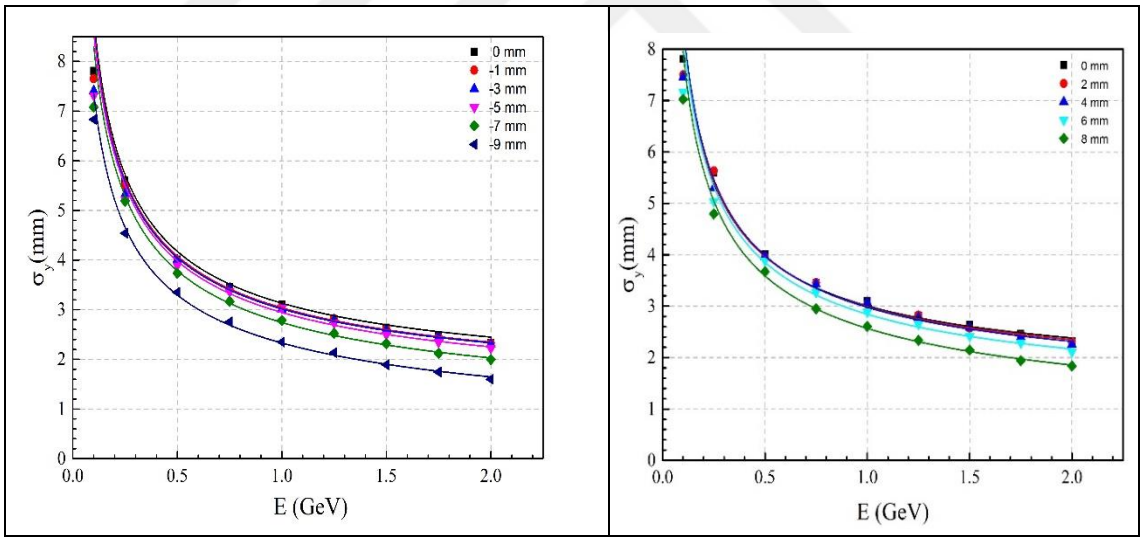

Figure 4.10. Obtained position resolutions in y coordinates at central 3×3 matrix LYSO as a function of electron energy. The solid lines represent the fits of the data. The error bars are smaller than the symbols presented.

Table 4.4. The fit parameters of position resolution for different incidence positions of electrons in y coordinates.

Impact Position [mm]	*a*	*b*
8	2.51 ± 0.08	0.54 ± 0.26
6	2.60 ± 0.11	1.15 ± 0.18
4	2.64 ± 0.13	1.36 ± 0.19
2	2.61 ± 0.13	1.45 ± 0.17
0	2.77 ± 0.05	1.31 ± 0.07
-1	2.73 ± 0.05	1.34 ± 0.07
-3	2.70 ± 0.05	1.33 ± 0.06
-5	2.68 ± 0.09	1.21 ± 0.15
-7	2.61 ± 0.08	0.84 ± 0.18
-9	2.33± 0.021	6.65E-5 ± 0

In order to calculate the two-dimensional position resolution σ_R, σ_x and σ_y can be used:

$$\sigma_R\,(mm) = \sqrt{\sigma_x^2 + \sigma_y^2} \tag{4.8}$$

As a result, the position resolution σ_R in two-dimension was calculated as

$$\sigma_R(mm) = \frac{(3.95 \pm 0.08)}{\sqrt{E}} \oplus (1.91 \pm 0.11) \tag{4.9}$$

at the center of the matrix.

Figure 4.11 exhibits the calculated position resolution in two-dimension as a function of the incident electron energy at the central crystal of the 3×3 LYSO matrix. These calculations were made for electron energies of at 0.5, 1, and 2 GeV. In addition, the variation of the position resolution with respect to the impact point of the incident electron can be seen more clearly in Figure 4.12.

Table 4.5. The fit parameters of position resolution for different incidence positions of electrons in two dimensions.

Impact Position [mm]	*a*	*b*
8	3.57± 0.10	0.82± 0.29
6	3.77± 0.15	1.54± 0.25
4	3.80± 0.18	1.95± 0.24
2	3.82± 0.18	2.02± 0.24
0	3.74± 0.18	2.16± 0.22
-1	3.73 ± 0.17	2.15± 0.20
-3	3.57 ± 0.21	2.23 ± 0.23
-5	3.79± 0.17	1.79 ± 0.25
-7	3.60 ± 0.15	1.39 ± 0.26
-9	3.31 ± 0.03	-6.7285E-4 ± 0

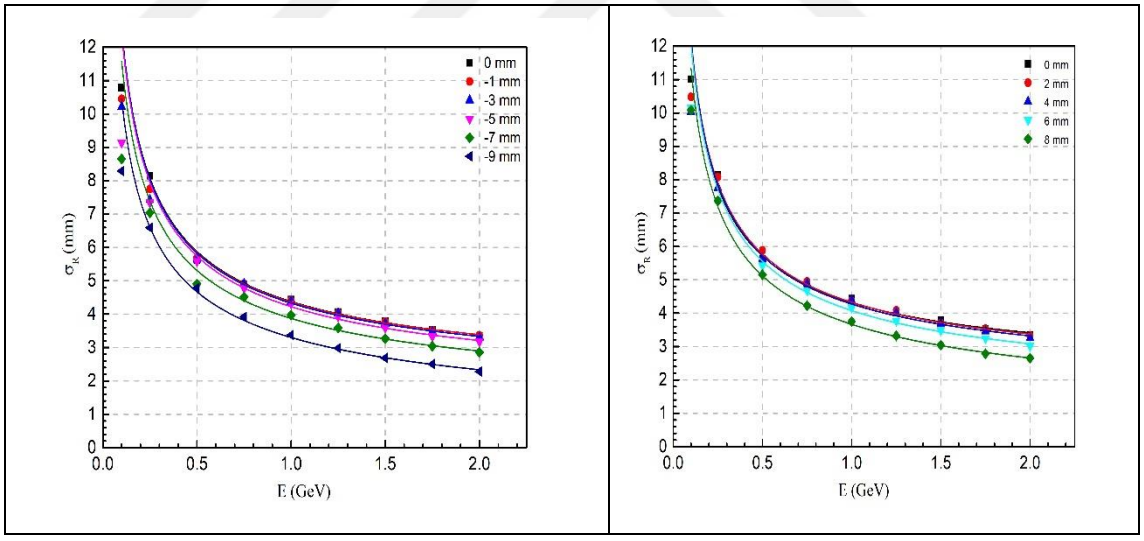

Figure 4.11. Obtained position resolution in two-dimensional as a function of electron energy.

To analyze the changing of the position resolution depending on the angle at which an electron collides with the crystal calorimeter, the incidence of the electron was turned by 5°, 10° and 15° relative to normal. The calculations were made for electron energies of 0.5, 1, and 2 GeV.

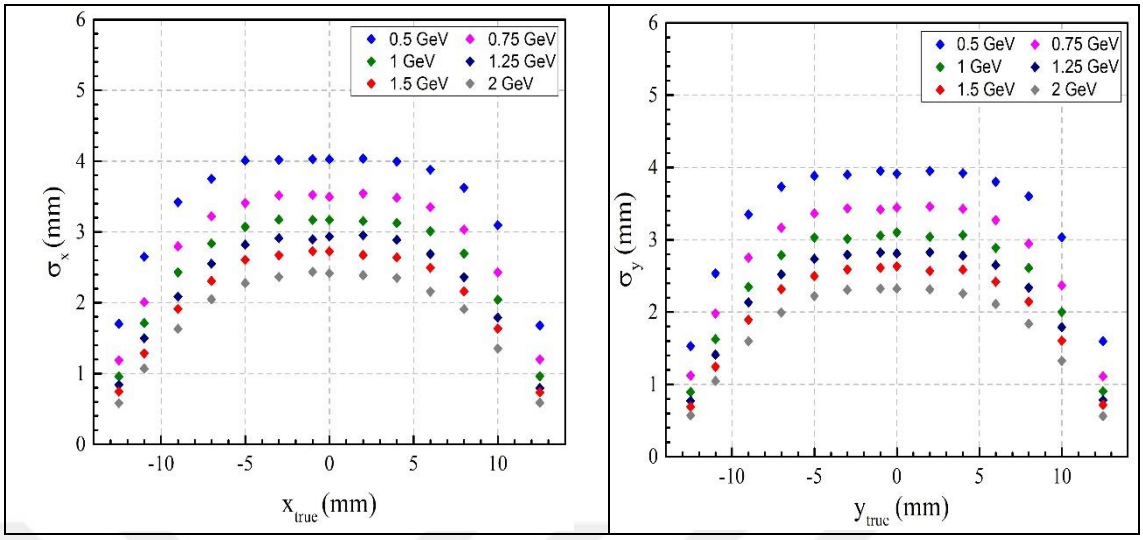

Figure 4.12. Calculated position resolutions as a function of electron impact position in the x and y coordinates.

For each incidence angle, the S-shape was calculated and fitted. For example, the S-like curve obtained for electrons sent to the calorimeter with 5-degree incident at 0.5 GeV is shown in Figure 4.13.

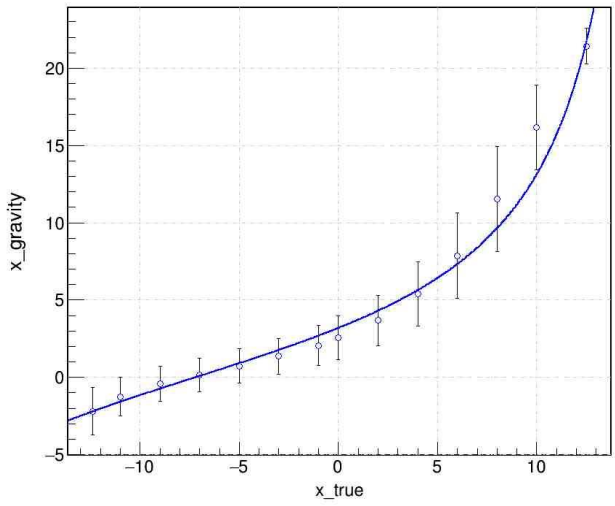

Figure 4.13. S-like curves for 5 degrees incident angle at 0.5 GeV.

The dependence of the position resolution on incident angle relative to the one at zero degrees incident angle for electron energies of 0.5 GeV, 1 GeV, and 2 GeV is shown in Figure 4.14. As can be seen from Figure 4.14 and Figure 4.15, position resolution is getting worse as electron incidence angle increases.

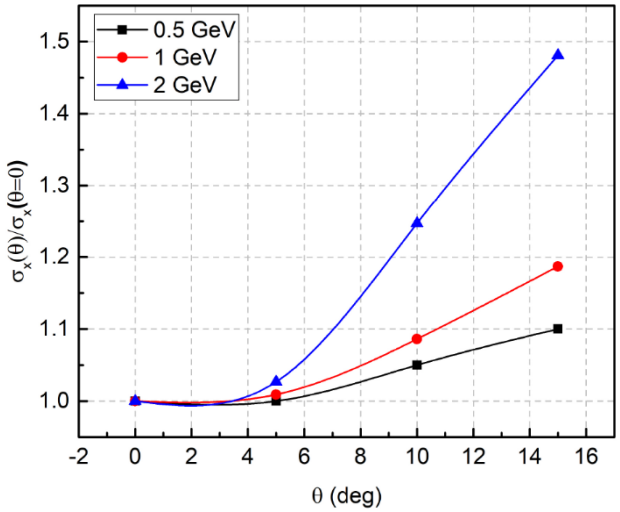

Figure 4.14. Variation of position resolution normalized to position resolution at zero degrees as a function of the electron incidence angle. The solid lines represent the fit results.

Table 4.6. Position resolution obtained for various incidence angles at the center of the central crystal. A sample of 10000 events was used for each energy.

	σ_x (mm)			
Energy (GeV)	0°	5°	10°	15°
0.5	4.025	4.049	4.341	4.213
1	3.169	3.196	3.440	3.759
2	2.415	2.480	3.012	3.577

By fitting the results in Table 4.6, we get:

$$\sigma_x(mm) = \frac{(2.64 \pm 0.12)}{\sqrt{E}} \oplus (1.60 \pm 0.21) \quad (4.10)$$

for normal incidence,

$$\sigma_x(mm) = \frac{(2.62 \pm 0.10)}{\sqrt{E}} \oplus (1.70 \pm 0.17) \quad (4.11)$$

for 5 degrees incidence,

$$\sigma_x(mm) = \frac{(2.55 \pm 0.08)}{\sqrt{E}} \oplus (2.38 \pm 0.10) \tag{4.12}$$

for 10 degrees incidence, and

$$\sigma_R(mm) = \frac{(1.82 \pm 0.07)}{\sqrt{E}} \oplus (3.32 \pm 0.05) \tag{4.13}$$

for 15 degrees incidence.

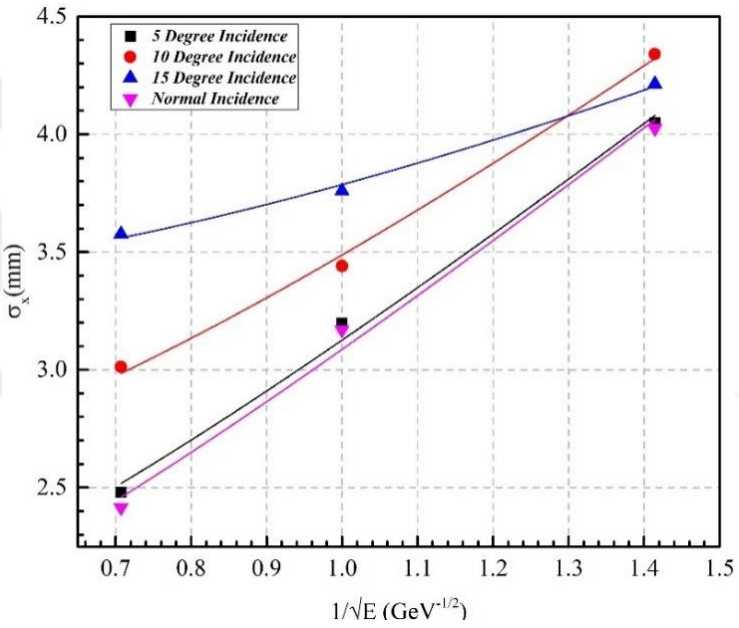

Figure 4.15. Calculated position resolutions as a function of inverse square root of electron's energy at the central LYSO crystal.

It can be seen from Figure 4.16 that the position resolution is not constant and change on the whole front face of the LYSO crystal and depends on the true position. This result originates to the fact that the transverse shape of the cascade profile which peaks strongly in the center. If the particle is sent directly to the crystal center, most of its energy is deposited in the central crystal. However, when a particle is sent at a non-zero angle to the central crystal, the energy deposited in the neighboring crystals increases. In this case, the center of gravity method gives better results. In the case of non-normal incidences such as, 5, 10, and 15 degrees, this becomes more important, resulting in

better position resolution on the right side of the LYSO crystal (Daskalakis & Markou, 1998).

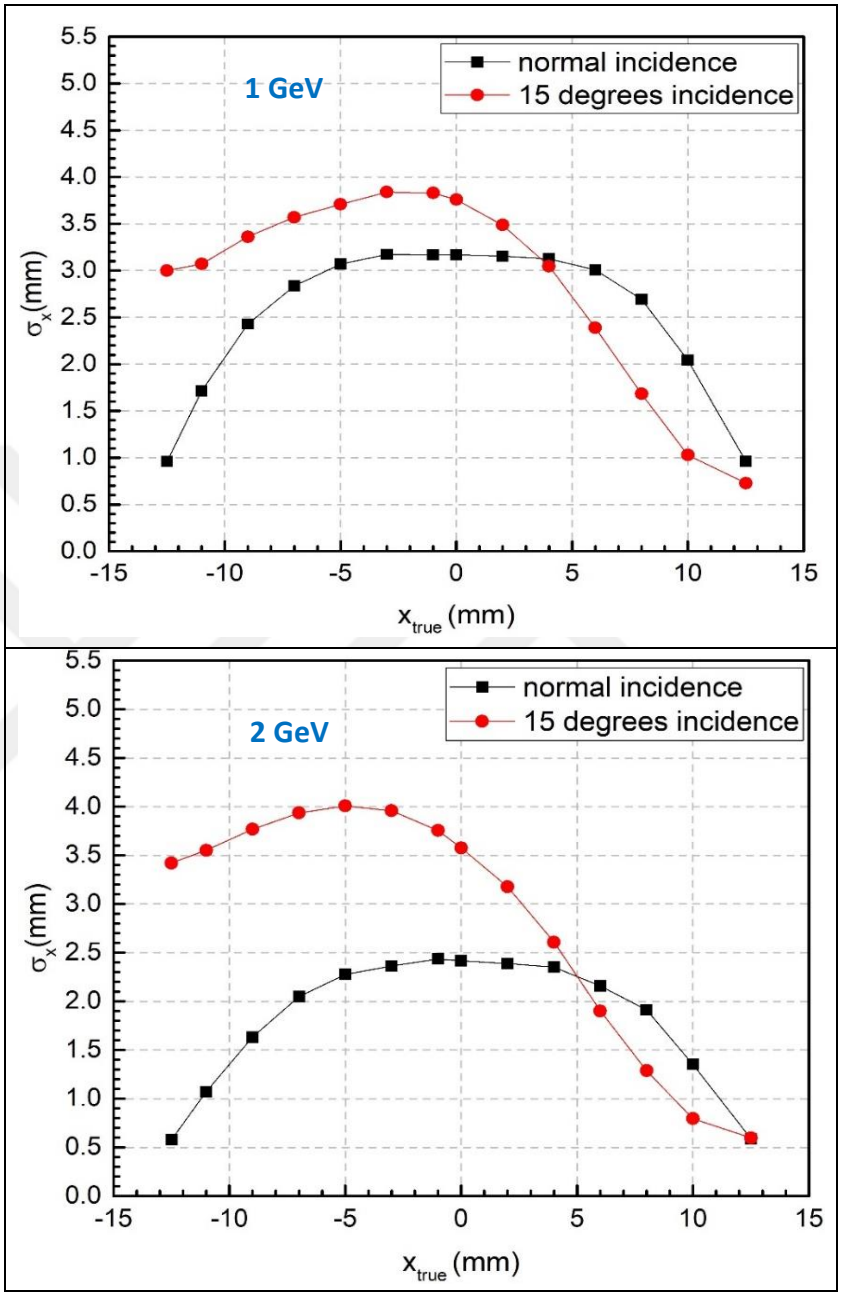

Figure 4.16. Position resolution versus the true position, for electron energies of 1 and 2 GeV at normal and 15 degrees incidence.

Lastly, in order to validate our GEANT4 code, crystal calorimeter model designed for the Coherent Muon to Electron Transition experiment (COMET) provided in (Oishi, 2014) was simulated. The electromagnetic calorimeter model involves 7×7 LYSO crystals with a feature of 120 mm in length and 20×20 mm^2 in cross section. The

position resolution of the electromagnetic calorimeter model was determined for the incident electrons by means of the center of gravity method. The achieved calculations are compatible with the data obtained from the experimental findings with insignificant difference at low energies as can be shown in Figure 4.17.

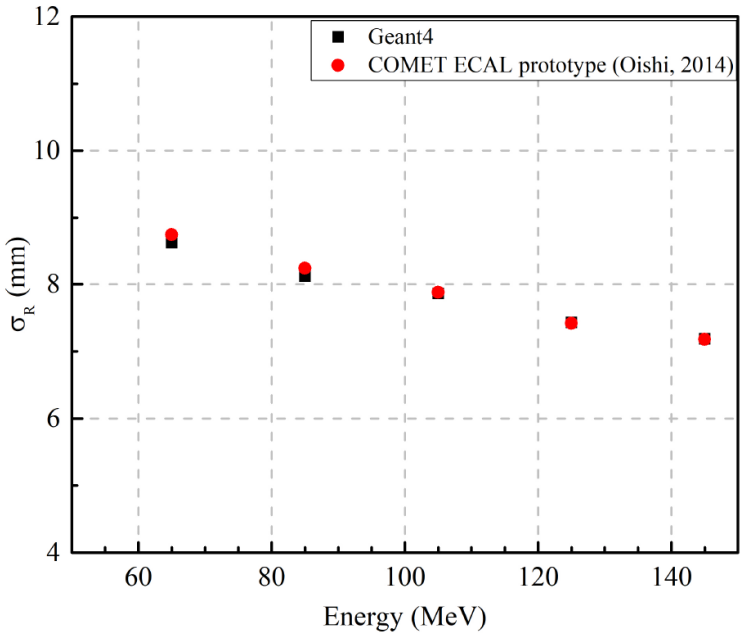

Figure 4.17. Position resolutions obtained from the GEANT4 simulation and the COMET ECAL prototype in Ref (Oishi, 2014).

5. CONCLUSION

In this thesis, the position resolution has been calculated for the geometry composed of LYSO crystals using the GEANT4 Monte Carlo simulation toolkit for the ECAL module of the proposed Turkish Accelerator Center Particle Factory (TAC-PF) detector. The gravity center method was applied to measure position resolution for electromagnetic cascade initiated by an electron in nine LYSO crystals in the form of a 3×3 matrix. The crystals have a cross-section of 25 × 25 mm^2 and a length of 200 mm. The calculations of position resolution were done at 14 different points (-12.5, -11, -9, -7, -5, -3, -1, 0, 2, 4, 6, 8, 10, 12.5) mm on the x and y axes to scan the entire surface of the crystal with incident electrons having energies of 0.1, 0.25, 0.5, 0.75, 1, 1.25, 1.5, 1.75 and 2 GeV (Figure 4.12). The position resolution has enhanced significantly with the correction of the S-curve. For an electron with an energy of 0.1 GeV hitting the center of the LYSO matrix, the position resolution in the x coordinate is 7.76 mm, and similarly in the y coordinate is 7.81 mm. As the electron energy increase, the position resolution improves which leads to the best position resolution at 2 GeV and was calculated to be 2.41 mm in the x coordinate and 2.32 mm in the y coordinate. The position resolution at the center of the matrix was parameterized as $\sigma_x(mm) = ((2.77 \pm 0.07)/\sqrt{E}) \oplus (1.46 \pm 0.10))$ in the x coordinate and a similar result was found for the y coordinate as expected. Two-dimensional position resolution was calculated and parameterized as $\sigma_R(mm) = ((3.95 \pm 0.08)/\sqrt{E}) \oplus (1.91 \pm 0.11))$. Also, by means of equation 4.1 and 4.2 for the x and the y coordinates using the fit parameters c, d, and e in Table 4.1 and 4.2, with minor adjustment, the impact position of an electron in similar sized LYSO calorimeters can be determined from gravity center of the energy depositions in the crystals. The position resolution is highly angle-dependent. In the case of 15-degree incidence the position resolution was parameterized as $\sigma_x(mm) = ((1.82 \pm 0.07)/\sqrt{E}) \oplus (3.32 \pm 0.05))$. The resolution at 15-degrees is lower than the normal incidence by a factor of 1.2 at 1 GeV and 1.5 at 2 GeV. However, since the incident electron is sent to the centeral crystal at different angles towards the right, and thus more energy is deposited in the neighboring crysals on the right, the position resolution on the right side of the crystal becomes better.

As an alternative way for determining the position resolution, the logarithmic weighted method, which uses logarithmic weights of the energy deposits in the crystals, can be applied. The results obtained from both methods can be compared with each other.

REFERENCES

Abashian, A., Gotow, K., Morgan, N., Piilonen, L., Schrenk, S., Abe, K., ...Wang, M. Z. (2002). The Belle detector. *Nuclear Instruments and Methods in Physics Research Section A: Accelerators, Spectrometers, Detectors and Associated Equipment*, *479*(1): 117–232. doi: 10.1016/S0168-9002(01)02013-7

Agostinelli, S., Allison, J., Amako, K. A., Apostolakis, J., Araujo, H., Arce, P., ... Zschiesche, D. (2003). GEANT4-a simulation toolkit. *Nuclear Instruments and Methods in Physics Research Section A: Accelerators, Spectrometers, Detectors and Associated Equipment*, *506*(3): 250–303. doi: 10.1016/S0168-9002(03)01368-8

Akrawy, M., Arnison, G. T. J., Batley, J. R., Bell, K. W., Brown, R. M., Carter, A. A., ... Ward, C. P. (1990). Development studies for the OPAL end cap electromagnetic calorimeter using vacuum photo triode instrumented leadglass. *Nuclear Instruments and Methods in Physics Research Section A: Accelerators, Spectrometers, Detectors and Associated Equipment*, *290*(1): 76–94. doi: 10.1016/0168-9002(90)90346-8

Aksoy, A., Cakır, O., Duran Yıldız, H., Yavas, O., Akkus, B., Ozkorucuklu, S., ... Algin, E. (2014). Turkish Accelerator Center: The Status and Road Map. *Proceedings of the 5th International Particle Accelerator Conference (IPAC2014)*, Dresden, Germany: 2921–2923. doi: 10.18429/JACoW-IPAC2014-THPRO027

Aksu, B., & Piliçer, E. (2017). Detector design studies for Turkish Accelerator Center. *AIP Conference Proceedings,* 1815(1): 060001. doi:10.1063/1.4976397

Alavi-Harati, A., Albuquerque, I. F., Alexopoulos, T., Arenton, M., Arisaka, K., Averitte, S., ... KTeV Collaboration. (1999). Observation of Direct CP Violation in K S, L→ π π Decays. *Physical Review Letters*, *83*(1): 22. doi: 10.1103/PhysRevLett.83.22

Altegoer, J., Anfreville, M., Angelini, C., Astier, P., Authier, M., Autiero, D., ... Vo, M. K. (1998). The NOMAD experiment at the CERN SPS. *Nuclear Instruments and Methods in Physics Research Section A: Accelerators, Spectrometers, Detectors and Associated Equipment*, *404*(1): 96-128. doi: 10.1016/S0168-9002(97)01079-6

Amaldi, U. (1981). Fluctuations in calorimetry measurements. *Physica Scripta*, *23*(4A): 409. doi:10.1088/0031-8949/23/4A/012

Ankara University, (2020). Türk Hızlandırıcı Merkezi. Access address: http://thm.ankara.edu.tr (Visited on 2.1.2020).

Balka, L., Coover, K., Diebold, R., Evans, W., Hill, N., Nodulman, L., ... Mikamo, S. (1988). The CDF central electromagnetic calorimeter. *Nuclear Instruments and Methods in Physics Research Section A: Accelerators, Spectrometers, Detectors and Associated Equipment*, *267*(2–3): 272–279. doi: 10.1016/0168-9002(88)90474-3

Batarin, V., Brennan, T., Butler, J., Cheung, H., Derevschikov, A., Fomin, Y., ... Yarba, J. (2003). Precision measurement of energy and position resolutions of the BTeV electromagnetic calorimeter prototype. *Nuclear Instruments and Methods in Physics Research Section A: Accelerators, Spectrometers, Detectors and Associated Equipment*, *510*(3): 248–261. doi: 10.1016/S0168-9002(03)01862-X

Bebek, C. (1988). A cesium iodide calorimeter with photodiode readout for CLEO II. *Nuclear Instruments and Methods in Physics Research Section A: Accelerators, Spectrometers, Detectors and Associated Equipment*, *265*(1–2): 258–265. doi:10.1016/0168-9002(88)91079-0

Bertolucci, S., Cordelli, M., Esposito, B., Curatolo, M., Giromini, P., Miscetti, S., ... Kautzky, H. (1988). The CDF central and endwall hadron calorimeter. *Nuclear Instruments and Methods in Physics Research Section A: Accelerators, Spectrometers, Detectors and Associated Equipment*, *267*(2–3): 301–314. doi: 10.1016/0168-9002(88)90476-7

Boutigny, D., Goy, C., Karyotakis, Y., Lees, J. P., Lees Rosier, S., Evangelista, C., ... Mallik, U. (1995). BaBar technical design report. Access address: http://www.slac.stanford.edu/cgi-wrap/getdoc/slac-r-457.pdf

Brun, R., Hagelberg, R., Hansroul, M., Lassalle, J.C. (1978). Simulation program for particle physics experiments, GEANT: user guide and reference manual, *CERN Document Server*. Access address: https://cds.cern.ch/record/118715 (visited on 2.1.2020).

Cem, S. (2006). NATIONAL GRID INITIATIVE IN TURKEY TR-Grid. *EGI SEE Workshop*, Athens, Greece, 11 pp. Access address: https://www.google.com/url?sa=t&rct=j&q=&esrc=s&source=web&cd=&cad=rja&uact=8&ved=2ahUKEwjWlrT28vxAhVgg_0HHf9A_EQFjAAegQIBxAD&url=https%3A%2F%2Findico.cern.ch%2Fevent%2F429895%2Fcontributions%2F1064295%2Fattachments%2F927066%2F1312393%2FTRGrid_Initiative_StatusApril_2006.pdf&usg=AOvVaw0x45fJlEsEY1E8B gasmGGP

Chaturvedi, U., Favara, A., Gataullin, M., Gratta, G., Kirkby, D., Lu, W., ... Zhu, R. (2001). Calibration of the L3 BGO calorimeter using an RFQ accelerator. *Nuclear Instruments and Methods in Physics Research Section A: Accelerators, Spectrometers, Detectors and Associated Equipment*, *461*(1–3): 376–377. doi:10.1016/S0168-9002(00)01248-1

CMS collaboration. (1997). The CMS electromagnetic calorimeter project. *Technical Design Report CMS*, CERN/LHCC 97-33, *CMS TDR, 4*.

D4Cordelli, M., Happacher, F., Martini, M., Miscetti, S., Sarra, I., Schioppa, M., & Stucci, S. (2011). CCALT: A crystal calorimeter for the KLOE-2 experiment. In *Journal of Physics: Conference Series*, 293(1): 012010). IOP Publishing. doi: 10.1088/1742- 6596/293/1/012010

Daskalakis, G., & Markou, C. (1998). *Monte Carlo studies on Position Resolution for the CMS ECAL calorimeter* (No. CMS-NOTE-1998-053). CERN-CMS-NOTE-1998–053. Retrieved from https://s3.cern.ch/inspire-prod-files-0/05706b51e731f998646da08c89647565

Desler, K., & Edwards, D. A. (2000). Accelerator physics of colliders. *The European Physical Journal. C., Particles and Fields*, *15*(1–4): 157–159. doi:10.1007/BF02683417

Eigen, G., Zhou, Z., Chao, D., Cheng, C., Echenard, B., Flood, K., ... Budano, A. (2013). A LYSO calorimeter for the Super B factory. *Nuclear Instruments and Methods*

in Physics Research Section A: Accelerators, Spectrometers, Detectors and Associated Equipment, *718*: 107–109. doi: 10.1016/j.nima.2012.11.100

Fabjan, C. W., & Gianotti, F. (2003). Calorimetry for particle physics. *Reviews of Modern Physics*, *75*(4): 1243. doi:10.1103/RevModPhys.75.1243

Fanti, V., Lai, A., Musa, L., Nappi, A., Setzu, M., Moore, R.W,... Taurok, A. (1999). A measurement of the transverse polarization of $\Lambda $-hyperons produced in inelastic p N-reactions at 450 GeV proton energy. *The European Physical Journal C-Particles and Fields*, *6*(2): 265–269. doi: 10.1007/s100529801045

Frass, W., & Wlaczak, R. (2009). Particle detectors, *Oxford Physics*. Access address: http://www2.physics.ox.ac.uk/sites/default/files/Detectors.pdf, 5 (visited on 17.4. 2020).

GEANT4 Collaboration. (2020). GEANT4 scope of application Introduction to GEANT4 10.7 documentation. *CERN*. Access address: https://geant4userdoc.web.cern.ch/UsersGuides/IntroductionToGeant4/html/IntroductionToG4.html#geant4-scope-of-application, (visited on 2.1. 2020).

Gell-Mann, M. (1962). Symmetries of Baryons and Mesons. Physical Review, 125(3), 1067–1084. doi:10.1103/physrev.125.1067

Gratta, G., Newman, H., & Zhu, R. Y. (1994). Crystal calorimeters in particle physics. *Annual Review of Nuclear and Particle Science*, *44*(1): 453–500. Access address: https://www.annualreviews.org/doi/pdf/10.1146/annurev.ns.44.120194 .0 02321

Group, T. Z. C., Behrens, U., Crittenden, J., Dierks, K., Drews, G., Engelen, J., ... Youngman, C. (1990). Test of the ZEUS forward calorimeter prototype. *Nuclear Instruments and Methods in Physics Research Section A: Accelerators, Spectrometers, Detectors and Associated Equipment*, 289(1–2): 115–138. doi: 10.1016/0168-9002(90)90253-3

Grupen, C., & Shwartz, B. (2008). Particle detectors. Cambridge Monographs on Particle Physics, Nuclear Physics and Cosmology. 2 edn. Cambridge University Press. doi:10.1017/CBO9780511534966

Hagiwara, K., Hikasa, K., Nakamura, K., Tanabashi, M., Aguilar-Benitez, M., Amsler, C. D., ... Zenin, O. V. (2002). Review of particle physics: Particle data group. *Physical Review D*, *66*(1 I), 100011-10001958. doi:10.1103/PhysRevD.66.010001

Kimble, T., Chou, M., & Chai, B. H. (2002). Scintillation properties of LYSO crystals. In *2002 IEEE Nuclear Science Symposium Conference Record.,* 3: 1434–1437. doi:10.1109/NSSMIC.2002.1239590

Koçak, F. (2010*). Kalorimetrede enerji çözünürlüğü [Energy resolution in calorimeter]*. (Ph.D. Thesis), Institute of Natural and Applied Sciences, Uludag University, Bursa, Turkey. Retrieved from https://tez.yok.gov.tr/UlusalTezMerkezi/TezGoster?key=iTkOhwevEenJZ3onUvs52g9T858WZHDJyslBJHPTZRNNFo43NuGQFDkWAJSFtyCG

Kocak, F. (2015). A Monte Carlo Study on Position Resolution of PWO Crystal. *Süleyman Demirel University Journal of Natural and Applied Sciences.,* 21(2): 296–298. Access address: https://dergipark.org.tr/en/ pub/sdufenbed/issue/ 34634/382548

Kocak, F., & Tapan, I. (2017). Simulation of LYSO crystal for the TAC-PF electromagnetic calorimeter. *Acta Physica Polonica A*, *131*(3): 527–529. doi:10.12693/APhysPolA.131.527

Mao, R., Zhang, L., & Zhu, R. Y. (2009). Gamma ray induced radiation damage in PWO and LSO/LYSO crystals. *2009 IEEE Nuclear Science Symposium Conference Record (NSS/MIC)*, (2045–2049). doi: 10.1109/NSSMIC.2 009.5402126

Mao, R., Zhang, L., & Zhu, R. Y. (2011). LSO/LYSO crystals for future HEP experiments. *Journal of Physics: Conference Series*, 293(1): 012004). doi: 10.1088/1742-6596/293/1/012004

Melcher, C. L., & Schweitzer, J. S. (1992). Cerium-doped lutetium oxyorthosilicate: a fast, efficient new scintillator. *IEEE Transactions on Nuclear Science*, *39*(4): 502–505. doi: 10.1109/23.159655

Moser, H. G. (2009). Silicon detector systems in high energy physics. *Progress in particle and nuclear physics*, *63*(1), p.186–237. doi:10.1016/j.ppnp.2008.12.002

Oishi, K. (2014). Development of electromagnetic calorimeter using GSO and LYSO crystals for the J- PARC muon-to-electron conversion search experiment. *2014 IEEE Nuclear Science Symposium and Medical Imaging Conference (NSS/MIC)*, 1–6. doi: 10.1109/NSSMIC.2014.7431243

Onur, T. (2005). TÜBİTAK ULAKBİM Yüksek Başarımlı Bilgi İşlem Merkezi ve TR-Grid Altyapısı. *National Grid Workshop*. Ankara. Access address: www.grid.org.tr (visited on 4.1. 2020).

Particle Data Group. (2016). Review of Particle Physics. *Chinese Physics*. C 40 (10): 100001, updated 2017. doi.org/10.1088/1674-1137/40/10/100001.

Salam, A. (1980). Gauge unification of fundamental forces. *Reviews of Modern Physics*, 52(3), 525. Doi:10.1103/RevModPhys.52.525

Sébastien, L. (2020). A practical introduction to the Geant4 Monte Carlo simulation toolkit. University of Bordeaux 1, Centre of Nuclear Studies of Bordeaux-Gradignan (CENBG), Lecture Notes: Bordeaux, France, 24 p. Retrieved from https://www.google.com/url?sa=t&rct=j&q=&esrc=s&source=web&cd=&ved=2ahUKEwiUiJyd4NDyAhUBs6QKHXFBBy4QFnoECAIQAQ&url=https%3A%2F%2Findico.in2p3.fr%2Fevent%2F147%2Fcontributions%2F19459%2Fattachments%2F15853%2F19456%2FGeant4-S.Incerti.doc&usg=AOvVaw3Z6uq8MpHeMONXH_1P9jKI (visited on 4.1. 2020).

Sirunyan, A. M., Tumasyan, A., Adam, W., Asilar, E., Bergauer, T., Brandstetter, J., ... & Dogra, S. (2017). Particle-flow reconstruction and global event description with the CMS detector. *Journal of Instrumentation*, 86. doi.org/10.1088/1748-0221/12/10/P10003

Soo, H. B. (2017). *Radioisotopes and Radiation Methodology*[Pdf]. Med Phys 4R06/6R03. Retrieved from https://www.science.mcmaster.ca/radgrad/images/6R06CourseResources/4RA3--4RB3-Lecture-Note1_Radioactivity_Revised.pdf

TRUBA Wiki Sayfası, (2020). Access address: http://wiki.truba.gov.tr/index.php?title=Ana_sayfa&oldid=1178#TRUBA_Hakk.C4.B1nda (Visited on 4.1. 2020).

Weinberg, S. (1980). Conceptual foundations of the unified theory of weak and electromagnetic interactions. *Science*, 210(4475), 1212-1218. doi:10.1126/science.210.4475.1212

Wigmans, R. (2000). *Calorimetry: Energy measurement in particle physics*. (Vol. 107). Oxford University Press. ISBN: 19 850296 6.

Wigmans, R. (2008). Energy measurement at the TeV scale. *New Journal of Physics*, *10*(2): 025003. Access address: https://iopscience.iop.org/article/10.1088/1367-2630/10/2/025003/pdf

Yavaş, Ö. (2012). The status and road map of Turkish Accelerator Center (TAC). *Journal of Physics: Conference Series.*, 347(1): 012008. Access address: https://iopscience.iop.org/article/10.1088/1742-6596/347/1/012008/pdf

Zhu, R. Y. (2006). Precision crystal calorimeters in high energy physics: past, present and future. *American Institute of Physics AIP Conference Proceedings*, 867(1), p. 61–75. doi:10.1063/1.2396939